

# Chapter 1

## Introduction

### 1.1 Textures of cholesteric liquid crystals

For a cholesteric liquid crystal with a given pitch, its texture is characterised by the direction of the helical axis. When the helical axis is perpendicular to the cell surface, the planar texture is obtained, as shown in Fig. 1.1(a). A microphotograph of the planar texture with domain boundary is shown in Fig. 1.1(b). When, on the other hand, the helical axis is more or less parallel to the cell surface, the focal conic texture is obtained, as shown in Fig. 1.2(a). A microphotograph of the focal conic texture is shown in Fig. 1.2(b). However, when the pitch of a cholesteric liquid crystal is long and the helical axis is parallel to the cell surface, the texture is called fingerprint texture, as shown in Fig. 1.3(a). Figure 1.3(b) shows a microphotograph of the fingerprint texture.

With the appropriate substrate surface treatment or dispersed polymer, the planar texture and focal conic texture can be stable at zero field. For a cholesteric liquid crystal with a positive dielectric anisotropy, the pitch can be elongated by applying an external field. When the applied field is larger than a critical field  $E_c = (\pi^2 / P_0) \times (K_{22} / \epsilon_0 \Delta \epsilon)^{1/2}$ , the helical structure is unwound. If the field is parallel to the helical axis, the field-induced homeotropic texture is obtained, as shown in Fig. 1.4(a). However, if the field is perpendicular to the helical axis, the field-induced

homogeneous texture is obtained, as shown in Fig. 1.4(b). In cholesteric liquid crystals, a transient planar texture forms during relaxation from the field-induced homeotropic texture. When the applied field is removed, the relaxation occurs that results in the formation of the transient planar texture, which is a Grandjean texture and possesses a pitch longer than the natural pitch, as shown in Fig. 1.4(c).

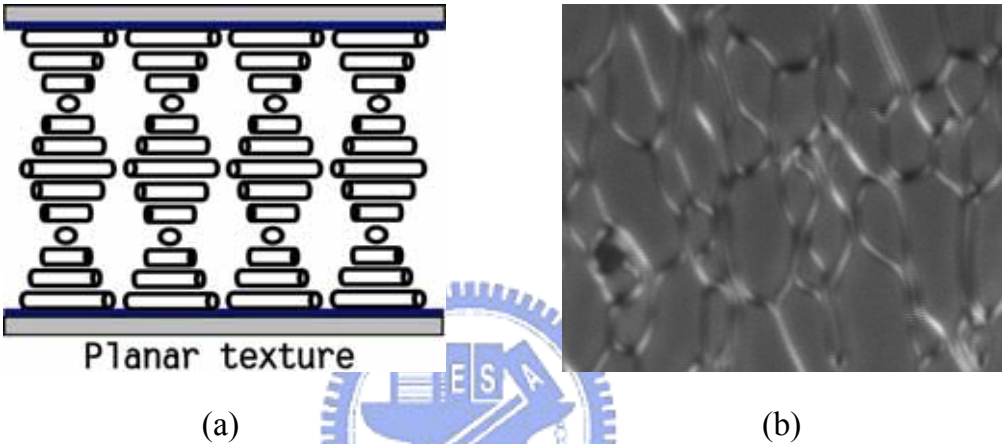


Figure 1.1 (a) Schematic structure of the planar texture. (b) Microphotograph of the planar texture.

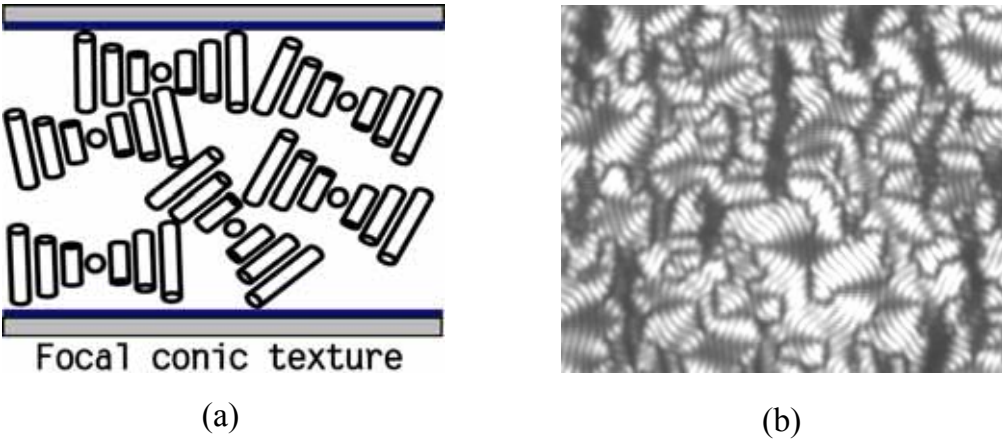


Figure 1.2 (a) Schematic structure of the focal conic texture. (b) Microphotograph of the focal conic texture.

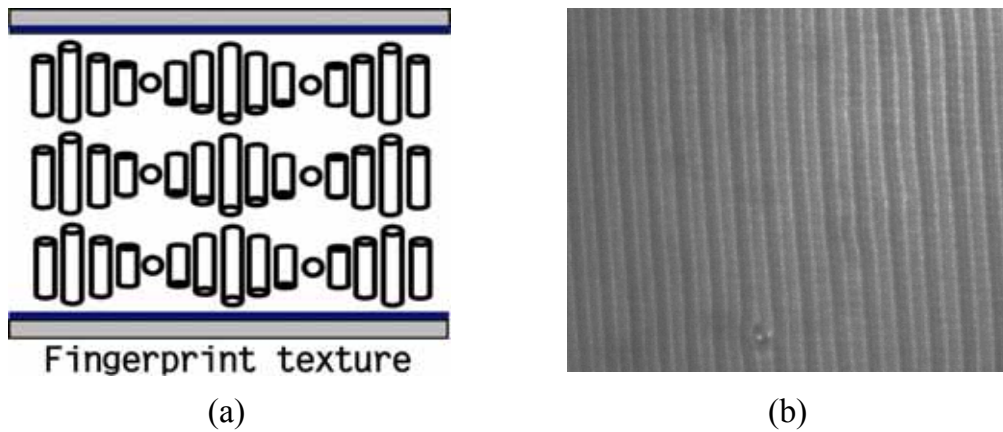


Figure 1.3 (a) Schematic structure of the fingerprint texture. (b) Microphotograph of the fingerprint texture.

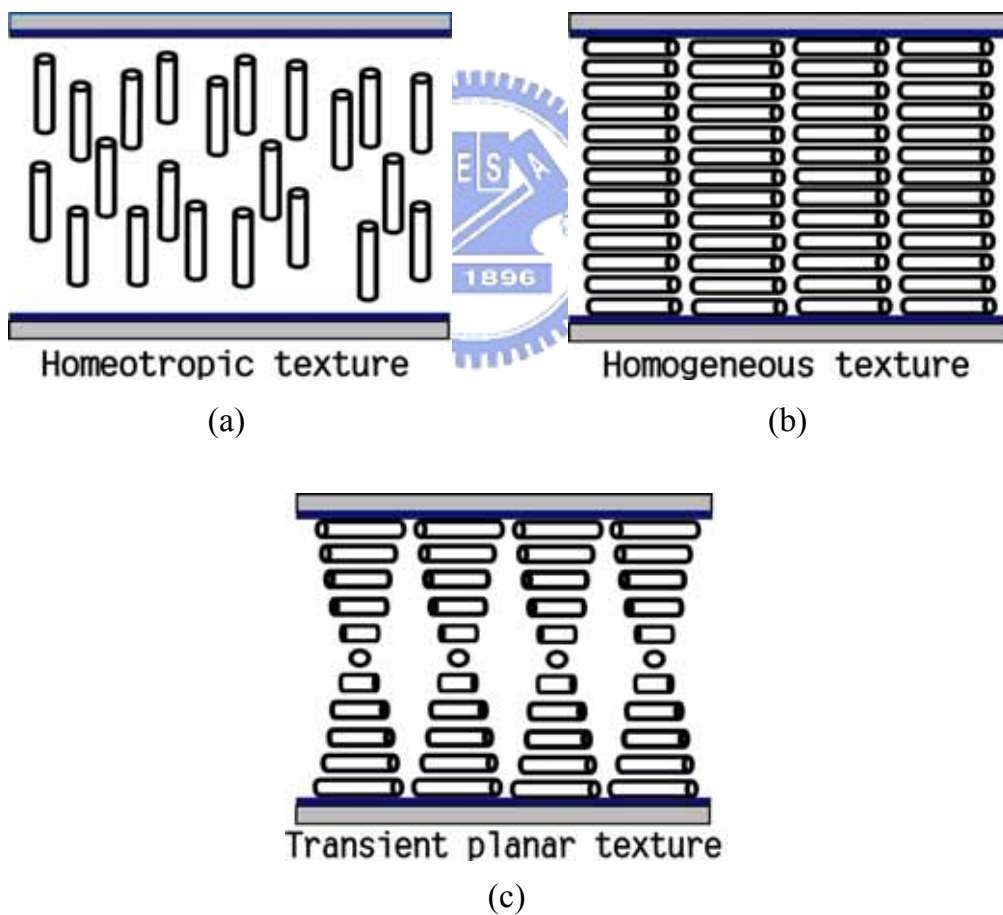


Figure 1.4 Schematic structures of (a) homeotropic texture, (b) homogeneous texture and (c) transient planar texture.

## 1.2 Optical properties of cholesteric textures

When a cholesteric liquid crystal is in the planar texture, there is a periodic variation of the refractive index along the cell normal direction. The refractive index oscillates between the ordinary refractive index  $n_o$  and the extraordinary refractive index  $n_e$  of the liquid crystals. The period is half of the natural pitch  $P_0$  because  $\bar{n}$  and  $-\bar{n}$  are equivalent. When the wavelength  $\lambda$  of incident light and  $P_0$  are comparable, the planar texture exhibits Bragg reflection at the wavelength  $\lambda_B$  with

$$m\lambda_B = P_0 \langle n \rangle \cos \theta . \quad (1.1)$$

Here,  $m$  is the diffraction order,  $\theta$  is the angle of light incidence and  $\langle n \rangle$  is the average refractive index of the medium. For light propagating along the helical axis, only the first-order Bragg reflection is possible. Therefore, the maximum of selective reflection occurs at  $\lambda_B = \langle n \rangle P_0$  for the normal incident light. The spectral width of the selective reflection band is equal to  $\Delta\lambda = P_0 \Delta n$ , where  $\Delta n = n_e - n_o$  is the birefringence of a nematic layer perpendicular to the helical axis. Circularly polarized light with the same handedness as the helical structure is reflected strongly because of the constructive interference of the light reflected from different positions, while circularly polarized light with the opposite handedness to the helical structure is not reflected because of the destructive interference of the light reflected from different positions. If the normally incident light is unpolarized, then the maximum reflection from the cholesteric liquid crystal is 50%. If the peak wavelength of the Bragg reflection lies in the visible spectrum, the planar texture will hence appear highly colored. In addition, the focal conic texture weakly scatters light in a forward direction, therefore is predominantly transparent in appearance. By painting the back of the cell with a black mask, the focal conic texture will therefore appear black.

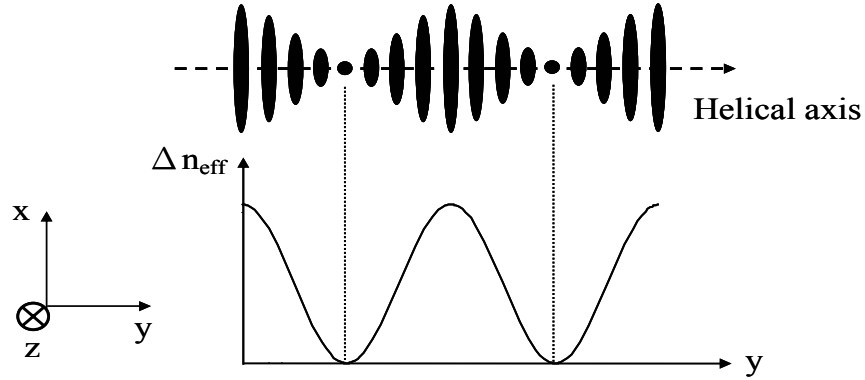


Figure 1.5 Schematic structure of the fingerprint texture which corresponds a periodic variation of the effective birefringence  $\Delta n_{\text{eff}} = (n_{\text{eff}} - n_o)$  when the light is incident along the z axis.

In the fingerprint texture, a cholesteric liquid crystal with a long pitch can be considered as a medium with a periodic gradient effective birefringence  $\Delta n_{\text{eff}}$ , as shown in Fig. 1.5. The effective birefringence changes between  $\Delta n (= n_e - n_o)$  and zero and the period is half of the pitch. This periodic effective birefringence will result in the periodicity in the phase and then causes a diffraction of the incident light. There are two main cases of interests, namely (a) the Raman-Nath diffraction and (b) the Bragg diffraction. Raman-Nath diffraction can occur when the helical axis is perpendicular to the incident beam direction, as shown in Fig. 1.6(a) and when the wavelength  $\lambda$  of the incident light, the grating period  $\Lambda$ , and the grating thickness (the thickness of the liquid crystal cell gap)  $d$  satisfy the condition  $Q \ll 1$ , where

$$Q = \lambda d / \Lambda^2. \quad (1.2)$$

The diffraction condition is given in general by

$$m\lambda = \Lambda \sin \theta_m, \quad (1.3)$$

where  $m$  is the diffraction order and  $\theta_m$  is the corresponding diffraction angle.

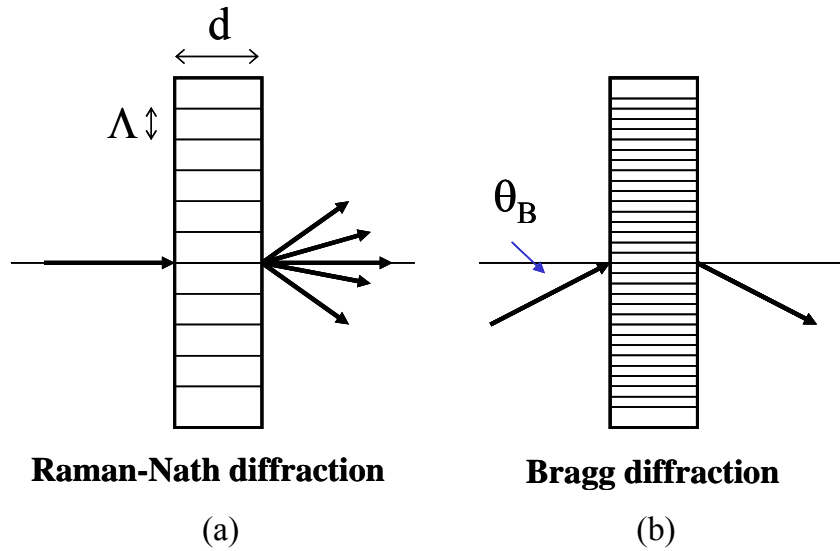


Figure 1.6 Geometry for (a) Raman-Nath diffraction and (b) Bragg diffraction.

As can be seen from Fig. 1.5, for the light with the polarization perpendicular to the helical axis, the refractive index is a periodic function of the coordinate  $y$  along the helical axis, namely  $n = n_{\text{eff}}$ . For the light with the polarization parallel to the helical axis, the refractive index is constant, namely  $n = n_0$ . Such a layer structure represents a polarization-sensitive phase grating: only the component of electric field vector that is perpendicular to the helical axis is diffracted.

On the other hand, when  $Q \gg 1$ , the Bragg diffraction occurs, as shown in Fig. 1.6(b), and the so-called Bragg angle  $\theta_B$  satisfies the condition

$$\theta_B = \arcsin(\lambda / 2\Lambda). \quad (1.4)$$

When the angle of the incidence light is equal to the Bragg angle, the intensity of the diffracted beam, which strongly depends on the angle of incidence, reaches a maximum. In other words, for each grating period  $\Lambda$ , the incident angle should be adjusted to satisfy the Bragg angle in order to obtain the maximum diffractive efficiency.

### **1.3 Aims of this research**

Cholesteric liquid crystals (ChLCs) are of considerable interest for display applications. The bistable characteristic of ChLCs eliminates the need for a constant refresh of the displays and permits image retention without any power, offering unprecedented energy savings in many applications. The naturally reflective property of ChLCs offers unmatched readability even in direct sunlight. Moreover, the cholesteric liquid crystal displays (Ch-LCDs) also exhibit high contrast ratio and high reflectance due to the reflective nature of ChLCs. Superior wide viewing angle is accomplished by the elimination of polarizers. Reflective Ch-LCDs do not require polarizers, color filters, back-lighting or active matrix substrates, therefore the manufacturing costs are minimized. On the other hand, the use of the passive matrix driving scheme also makes this technology particularly suitable for large area applications because it ensures that the largest possible aspect ratio is achieved, hence maximizing the total reflectance of the displays. In the very near future Ch-LCDs could form the ideal choice for low power sign board applications and hand held applications, such as cell phones and e-books.

Nevertheless, the switching time of the Ch-LCDs is relatively long. The typical frame update time using standard passive matrix driving techniques lies in the region of 10 ms per row. In order to enable the rapid updating of the Ch-LCDs and to design driving schemes, it is essential to understand the mechanisms of texture transitions in ChLCs. However, it is very hard to investigate the mechanisms of texture transitions in ChLCs, because it involves the complex evolution of director configurations during the texture transitions. Therefore, the three-dimensional simulation program based on the finite element method is developed to investigate



the dynamics of texture transitions in ChLCs. On the basis of the understanding for the mechanisms of texture transitions, the design of driving schemes can be made.

In recent years, interest in ChLCs has emerged not only for the applications of bistable Ch-LCDs but also for the applications of light modulators. The fingerprint texture with periodic helical twist structure, as shown in Fig. 1.5, is capable of Raman-Nath or Bragg diffraction, depending on the value of  $Q$  in equation (1.2). For most cholesteric diffractive devices, the initial state is a field-free planar texture. The dielectric coupling of the cholesteric structure with the external electric field creates the fingerprint texture, as shown in Fig. 1.3. Once the fingerprint texture is formed, the period is switchable by changing the applied electric field. In addition, the in-plane grating orientation strongly depends on  $\phi$ , the angle between the rubbing directions of two plates, and  $d/P_0$  ratio in a planar-aligned cholesteric liquid crystal cell. Experimental evidence has shown that the cell with  $\phi = 0^\circ$  exhibits no more than two possible striped orientations in the fingerprint texture. The striped orientation is either parallel or perpendicular to the rubbing direction, depending on the  $d/P_0$  ratio. For the cell with  $\phi = 90^\circ$ , the striped orientation makes an angle of  $45^\circ$  or  $135^\circ$  with one of the rubbing directions. In other words, for the cell with fixed angle  $\phi$  and  $d/P_0$  ratio, only one striped orientation is obtained.

In order to design cholesteric phase gratings with zero-field stable fingerprint texture and tunable striped orientation as well as striped period, it is essential to understand the formation mechanism of the fingerprint texture during the texture transition. On the basis of this understanding, the cholesteric phase gratings with the field-tunable grating orientation and grating period can be realized.



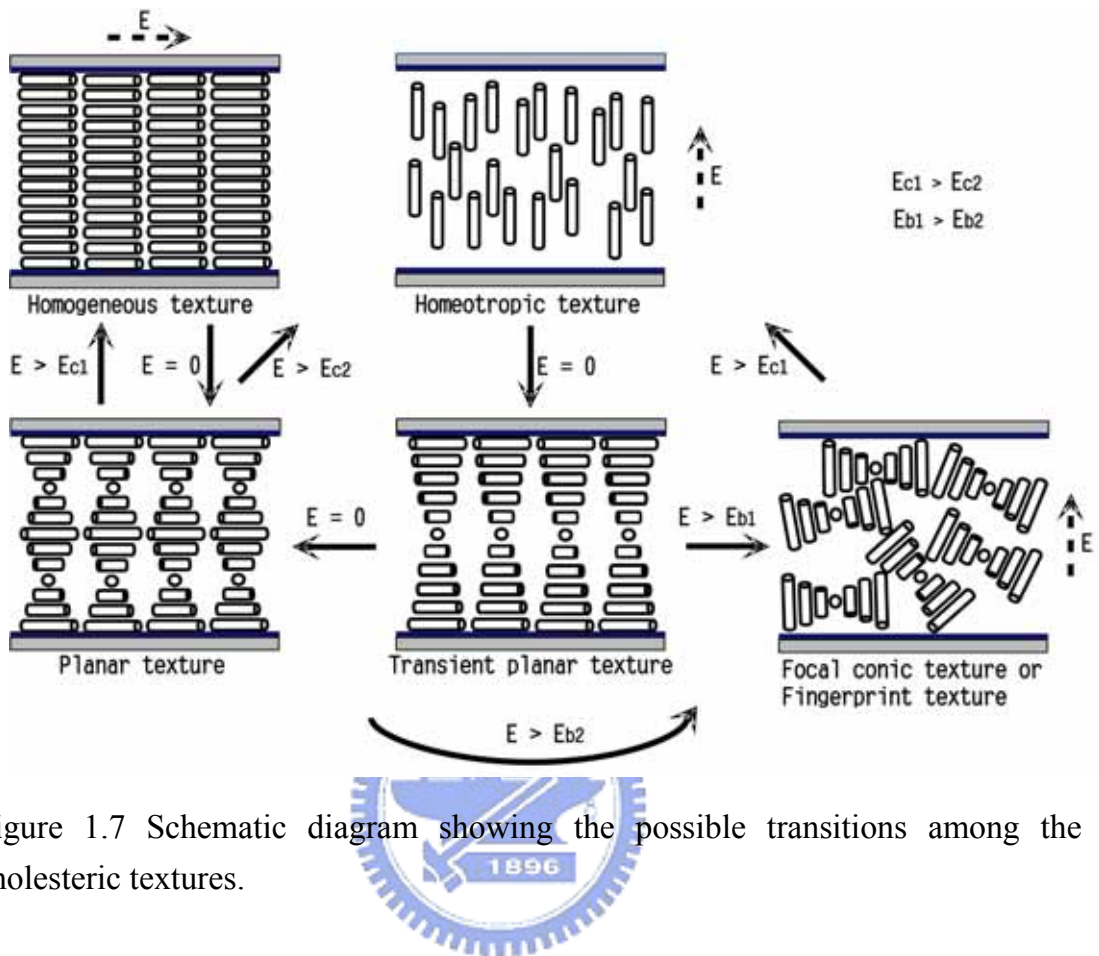


Figure 1.7 Schematic diagram showing the possible transitions among the cholesteric textures.

As illustrated in Figs. 1.1-1.4, ChLCs exhibit many textures which are determined by the surface anchoring, the cell thickness and the applied field. There are many possible transitions among these textures, as shown in Fig. 1.7, where  $E_{c1}$ ,  $E_{c2}$ ,  $E_{b1}$  and  $E_{b2}$  are threshold voltage of different texture transitions. These texture transitions are very interesting and are of importance for both fundamental science and applications. In order to investigate the dynamics of texture transitions, the basic theory and algorithm of simulation for modeling a ChLC system are discussed in chapter 2. In chapter 3, the dynamics of the homeotropic-planar texture transition in a planar-aligned cholesteric liquid crystal cell is numerically investigated and experimentally confirmed. Furthermore, the effect of bias waveforms on the

homeotropic-planar texture transition is discussed in chapter 4. On the basis of this knowledge, a bias waveform is designed to reduce the long relaxation time. In chapter 5, we numerically investigate the dynamics of the homogeneous-planar texture transition in a planar-aligned cholesteric liquid crystal cell. Moreover, the formation mechanism of the elastic-induced Helfrich deformation is reported. The electric-field-induced periodic modulated textures observed during the planar-focal conic texture transition in a planar-aligned cholesteric liquid crystal cell are described in chapter 6. In chapter 7, we observed the stripe formation during the homeotropic-fingerprint texture transition in homeotropic-aligned cholesteric liquid crystal cells with patterned electrode configurations. In this work, the cholesteric phase grating with the field-controllable grating orientation and grating period is realized and the operational mechanism of this device is presented. Finally, in chapter 8, summary and conclusions are made.



# Chapter 2

## Theory and Numerical Method

### 2.1 Theory

#### 2.1.1 Continuum theory of liquid crystals

In this section, we model the liquid crystal system based on the continuum theory which comes from the assumption that the director field is continuous over all space. Under this assumption, the average orientation of liquid crystal molecules in a local area can be denoted as a “director”. However, defects containing isotropic cores do not meet this assumption. Therefore, it is very hard to accurately predict the configuration of a defect with an isotropic core by the model based on the continuum theory. To accurately model the behavior of systems that include defects having isotropic cores, the rigorous Landau-de Gennes theory can be used [1]. This theory uses the order parameter tensor and can phenomenally explain the nematic-isotropic phase transition. In this thesis, we focus on the continuum theory which is the most commonly used to model the liquid crystal system.

#### 2.1.2 Elastic free energy

The elastic free energy is a measure of elastic stresses on the system. An elastic free energy of zero occurs when the directors are in the undisturbed state. For a nematic liquid crystal, this results in a configuration with all directors aligned parallel to each other, as shown in Fig 2.1(a).

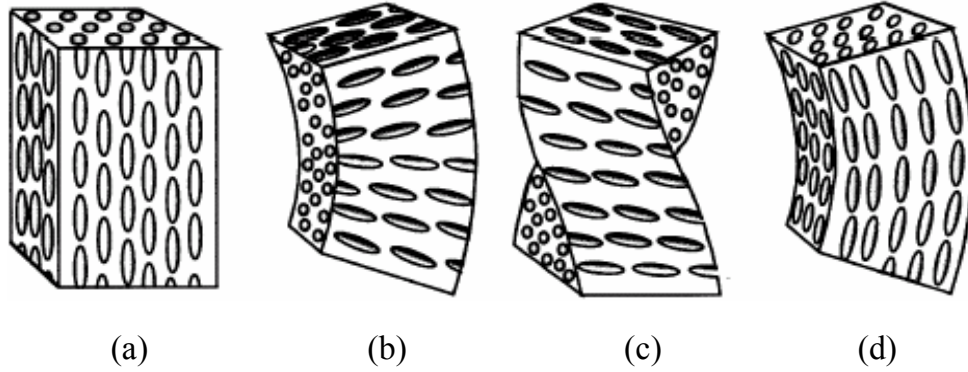


Figure 2.1 The equilibrium configuration of nematic liquid crystals is shown in (a). There are three types of elastic deformations: (b) splay, (c) twist, (d) bend.

Under the assumption of continuum theory, the Frank-Oseen theory is widely used to represent the elastic free energy of the liquid crystal system [2-4]. For an isothermal deformation of an incompressible *nematic* liquid crystal fluid, the expression of the elastic free energy density  $f_{lc}$  in terms of the director  $\bar{n}$  is given by

$$f_{lc} = \frac{1}{2} K_{11} (\nabla \cdot \bar{n})^2 + \frac{1}{2} K_{22} (\bar{n} \cdot \nabla \times \bar{n})^2 + \frac{1}{2} K_{33} (\bar{n} \times \nabla \times \bar{n})^2, \quad (2.1)$$

where  $K_{11}$ ,  $K_{22}$ ,  $K_{33}$  are elastic constants for splay, twist and bend, respectively, associated with three types of deformations illustrated in Fig 2.1. The first term  $(\nabla \cdot \bar{n})$  is for the splay deformation, the second term  $(\bar{n} \cdot \nabla \times \bar{n})$  is for the twist deformation and the third term  $(\bar{n} \times \nabla \times \bar{n})$  is for the bend deformation. In the ground state,  $f_{lc} = 0$ , thus  $\nabla \cdot \bar{n} = 0$ ,  $\bar{n} \cdot \nabla \times \bar{n} = 0$  and  $\bar{n} \times \nabla \times \bar{n} = 0$ ; that is, the director is unidirectional in space. Moreover, two other elastic constants  $K_{13}$  and  $K_{24}$ , related to the splay-bend deformation  $[\nabla \cdot (\bar{n} \nabla \cdot \bar{n})]$  and saddle-splay deformation  $[\nabla \cdot (\bar{n} \nabla \cdot \bar{n} + \bar{n} \times \nabla \times \bar{n})]$ , respectively, sometimes appear in the equation for the elastic free energy density. However, when the free energy contains the  $K_{13}$  term, it

can always be reduced; that is, there is no energy minimum [4]. Hence, the  $K_{13}$  term is usually ignored. For the  $K_{24}$  term, the free energy related to this term can be transposed from a volume integral to a surface integral [5]. Therefore, the  $K_{24}$  term can also be neglected when the anchoring energy on the surface is assumed to be sufficiently strong.

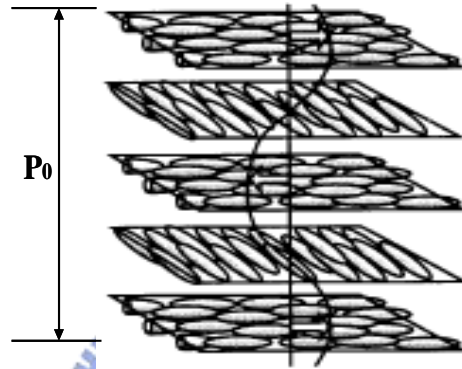


Figure 2.2 The structure of a cholesteric phase. The pitch is defined as the distance needed for the directors to twist  $360^\circ$  in space.

In the *cholesteric* (chiral nematic) liquid crystals, usually obtained by doping a small quantity of chiral molecules to a nematic liquid crystal, the liquid crystal molecules twist about their helical axis [6]. The distance along the helical axis for the directors to rotate  $360^\circ$  is called the pitch and is denoted by  $P_0$ , as shown in Fig. 2.2. To account this natural twist, equation 2.1 is modified as

$$f_{lc} = \frac{1}{2} K_{11} (\nabla \cdot \bar{n})^2 + \frac{1}{2} K_{22} (\bar{n} \cdot \nabla \times \bar{n} + q_0)^2 + \frac{1}{2} K_{33} (\bar{n} \times \nabla \times \bar{n})^2, \quad (2.2)$$

here,  $q_0 (=2\pi/P_0)$  is the chiral parameter and it represents the chirality of the system. The sign of  $q_0$  determines the handedness of the twist: a positive sign corresponds to

a right-hand twist and a negative sign corresponds to a left-hand twist. In the ground state,  $\nabla \cdot \bar{n} = 0$ ,  $\bar{n} \times \nabla \times \bar{n} = 0$  and  $\bar{n} \cdot \nabla \times \bar{n} = -q_0 \neq 0$ ; that is, the director field is no longer a uniform configuration in space but a twist structure, as shown in Fig. 2.2.

### 2.1.3 Electric free energy

In this section, we discuss the interaction between liquid crystals and electric field. Here, a liquid crystal with rod-like shape is considered and the nematic phase is uniaxial. There are two dielectric constants for rod-like director. One is the dielectric constant  $\epsilon_{\parallel}$  which is measured under the electric field parallel to the director. The other is the dielectric constant  $\epsilon_{\perp}$  which is measured under the electric field perpendicular to the director. The dielectric anisotropy  $\Delta\epsilon$  is defined as  $\epsilon_{\parallel} - \epsilon_{\perp}$ . When an electric field is applied to a liquid crystal, the liquid crystal becomes polarized and then an induced dipole forms. This effect is called *polarization* and is denoted as  $\bar{P}$  (dipole moment per unit volume) [7].

For linear dielectrics, the polarization is proportional to the electric field and is given by

$$\bar{P} = \epsilon_0 \chi_e \bar{E}, \quad (2.3)$$

where  $\epsilon_0$  is the permittivity of free space and is equal to  $8.854 \times 10^{-12} \text{ C}^2/\text{Nm}^2$ ,  $\chi_e$  is the electric susceptibility of the medium, and  $\bar{E}$  is the total field inside the medium and has units N/C or V/m. So the polarization has units of  $\text{C}/\text{m}^2$ , in accordance with its definition as the dipole moment (Cm) per unit volume ( $\text{m}^3$ ). By assuming the liquid crystal material to be a linear dielectric medium, the electric free energy density in an electric field  $\bar{E}_0$  caused by static charges is expressed as the following equation, [8]:

$$\begin{aligned}
f_e &= -\frac{1}{2} \bar{\mathbf{P}} \cdot \bar{\mathbf{E}}_0 \\
&= -\frac{1}{2} (\bar{\mathbf{P}}_{\parallel} \cdot \bar{\mathbf{E}}_0 + \bar{\mathbf{P}}_{\perp} \cdot \bar{\mathbf{E}}_0) \\
&= -\frac{1}{2} E_0 (P_{\parallel} \cos \theta + P_{\perp} \sin \theta) \\
&= -\frac{1}{2} E_0 \varepsilon_0 (\chi_{e_{\parallel}} E_{\parallel} \cos \theta + \chi_{e_{\perp}} E_{\perp} \sin \theta) \\
&= -\frac{1}{2} E_0 E \varepsilon_0 (\chi_{e_{\parallel}} \cos^2 \theta + \chi_{e_{\perp}} \sin^2 \theta) \\
&= -\frac{1}{2} E_0 E \varepsilon_0 (\varepsilon_{\parallel} \cos^2 \theta + \varepsilon_{\perp} \sin^2 \theta - 1) \\
&= -\frac{1}{2} E_0 E \varepsilon_0 (\varepsilon - 1) \\
&= -\frac{1}{2} E_0 D + \frac{1}{2} \varepsilon_0 E_0 E.
\end{aligned} \tag{2.4}$$

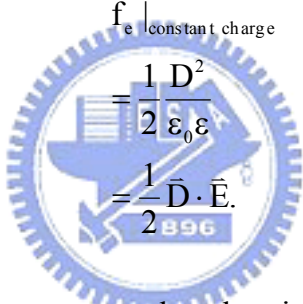
Here  $\theta$  is the angle between electric field and director,  $D$  is the electric displacement, and  $\varepsilon$  is the dielectric constant of the material. Equations  $\bar{\mathbf{D}} = \varepsilon_0 \varepsilon \bar{\mathbf{E}}$  and  $\varepsilon = 1 + \chi_e$  are used to derive equation (2.4).

Now we consider two physical systems which are frequently used to model the liquid crystal systems, that is, the constant charge system and constant voltage system. For the constant charge system, the voltage source is not connected to the liquid crystal system; in other words, it is a closed system and the electric energy cannot be injected to or rejected from the system, that is, electric charges on the cell electrodes are kept constant ideally, yielding  $\bar{\mathbf{D}} = \bar{\mathbf{D}}_0$ . Therefore, the electric energy density in equation (2.4) can be rewritten as



$$\begin{aligned}
f_e |_{\text{constant charge}} &= -\frac{1}{2} E_0 D + \frac{1}{2} \epsilon_0 E_0 E \\
&= -\frac{1}{2} \frac{D_0}{\epsilon_0} D + \frac{1}{2} D_0 \frac{D}{\epsilon_0 \epsilon} \\
&= -\frac{1}{2} \frac{D^2}{\epsilon_0} \left(1 - \frac{1}{\epsilon}\right).
\end{aligned} \tag{2.5}$$

Note the first term is not concerned with the director orientation, implying that it is a constant value for the energy of the system and can be dropped. Thus equation (2.5) becomes



$$\begin{aligned}
f_e |_{\text{constant charge}} &= \frac{1}{2} \frac{D^2}{\epsilon_0 \epsilon} \\
&= \frac{1}{2} \vec{D} \cdot \vec{E}.
\end{aligned} \tag{2.6}$$

For the constant voltage system, the electric source is connected, giving the system an open one, where the electric charge can be injected or ejected synchronously with the change of director distribution even if the applied voltage is kept constant. In this case, we consider the contribution of the second term in equation (2.4) to the electric free energy of the system, so we have

$$\begin{aligned}
F &= \int f \, dV \\
&= \frac{1}{2} \epsilon_0 E_0 \int E \, dl. \\
&= \frac{1}{2} \epsilon_0 E_0 v.
\end{aligned} \tag{2.7}$$

Similarly, this is a constant value and does not affect the director contribution at all. Therefore, the electric free energy density of the system can be rewritten as

$$\begin{aligned} f_e \Big|_{\text{constant voltage}} \\ = -\frac{1}{2} \bar{\mathbf{D}} \cdot \bar{\mathbf{E}}. \end{aligned} \quad (2.8)$$

Finally, we conclude that, under the constant charge condition, the electric free energy density is represented as  $1/2(\bar{\mathbf{D}} \cdot \bar{\mathbf{E}})$  which is used in the ‘‘Helmholtz’’ free energy representation. On the other hand, under the constant voltage condition, the electric free energy density is represented as  $-1/2(\bar{\mathbf{D}} \cdot \bar{\mathbf{E}})$  which is used in the ‘‘Gibbs’’ free energy representation. According to the statistical thermodynamics theory, the Helmholtz free energy has a minimum value in a constant charge system, whereas the electric Gibbs free energy has a minimum value in a constant voltage system [9,10].

The electric free energy density can also be represented in terms of the applied voltage  $v$  instead of the electric displacement  $\bar{\mathbf{D}}$ . In the right-handed Cartesian coordinates, the dielectric tensor can be rewritten as

$$\varepsilon_{ij} = \varepsilon_{\perp} \delta_{ij} + \Delta\varepsilon n_i n_j, \quad (2.9)$$

where  $\delta_{ij}$  is Kronecker’s delta (  $\delta_{ij} = 1$  when  $i=j$ ; otherwise  $\delta_{ij} = 0$ ;  $i, j = 1\sim 3$  ). Under the application of an electric field, the electric displacement inside the liquid crystal medium is given by  $D_i = \varepsilon_0 \varepsilon_{ij} E_j$  and from equation (2.9), we obtain

$$D_i = \varepsilon_0 \varepsilon_{\perp} E_i + \varepsilon_0 \Delta\varepsilon (\bar{\mathbf{n}} \cdot \bar{\mathbf{E}}) n_i.$$

or

$$\bar{\mathbf{D}} = \varepsilon_0 \varepsilon_{\perp} \bar{\mathbf{E}} + \varepsilon_0 \Delta \varepsilon (\bar{\mathbf{n}} \cdot \bar{\mathbf{E}}) \bar{\mathbf{n}}. \quad (2.10)$$

In terms of  $\bar{\mathbf{E}} = -\nabla v$ , we have

$$\begin{aligned} & \frac{1}{2} \bar{\mathbf{D}} \cdot \bar{\mathbf{E}} \\ &= \frac{1}{2} (\varepsilon_0 \varepsilon_{\perp} \bar{\mathbf{E}}^2 + \varepsilon_0 \Delta \varepsilon (\bar{\mathbf{n}} \cdot \bar{\mathbf{E}})^2) \\ &= \frac{1}{2} (\varepsilon_0 \varepsilon_{\perp} (-\nabla v)^2 + \varepsilon_0 \Delta \varepsilon (\bar{\mathbf{n}} \cdot (-\nabla v))^2). \end{aligned} \quad (2.11)$$

#### 2.1.4 Surface free energy

The directors at the surface are usually anchored along an energy favorable orientation, called the “easy direction” or “easy axis” which is usually determined by the rubbing direction. When the director at the surface deviates from the easy direction, the surface energy has to be added to the energy of the system. The interaction between the director and surface is characterized by the “anchoring strength” or “anchoring energy”, which is a measure of how rigidly the director at the surface is fixed at its easy axis. For convenience, the dimensionless surface parameter  $\lambda_s$  is introduced:

$$\lambda_s = \frac{\pi K_{11}}{Ad}, \quad (2.12)$$

here  $A$  is the anchoring strength and  $d$  is the cell gap. The larger the anchoring strength, the smaller the surface parameter, and for strong anchoring condition, the surface parameter  $\lambda_s$  equals to zero because the anchoring strength  $A$  goes to infinity.

There are two kinds of anchoring energy capable of describing the interaction between the surface and director. One is the polar anchoring energy which is associated with how much energy is required to pull the director away from the surface. The other is azimuthal anchoring energy which is associated with how much energy is required to rotate the director at the surface. Rapini and Papoular built a simple phenomenological expression for the surface free energy density [11]:

$$f_s = \frac{1}{2} A_p \sin^2 \Delta\alpha + \frac{1}{2} A_a \sin^2 \Delta\phi, \quad (2.13)$$

here  $A_p$  and  $A_a$  denote the polar and azimuthal anchoring strengths, respectively.  $\Delta\alpha$  and  $\Delta\phi$  are the deviation angles of the director at the surface from the easy axis at the polar and azimuthal directions, respectively. Note that equation (2.13) is obtained under the assumption that the anchoring energy of the surface can be decoupled into polar and azimuthal anchoring energy, respectively. This is valid only when the coupling between polar and azimuthal anchoring energy is not very strong. However, in real situations, they couple with each other, therefore the interfacial energy density in equation (2.13) can be generalized by a “simple” coupling between polar and azimuthal interfacial free energy densities as the following equation [12]:

$$f_s = \frac{1}{2} A_p \sin^2 \Delta\alpha + \frac{1}{2} A_a \sin^2 \Delta\phi \cos^2 \alpha, \quad (2.14)$$

where  $\alpha$  is the pretilt angle of the director at the surface. In recent years, many attempts had been made to generalize the R-P surface energy model [13-16].

### 2.1.5 Total free energy

The total free energy of the liquid crystal system is obtained by adding the bulk free energy, which is the integral of the Gibbs free energy density  $f_g$  over the volume of the system, and surface free energy, which is the integral of the surface free energy density  $f_s$  over the surface of the volume, and is given by

$$F = \int f_g dV + \int f_s dS, \quad (2.15)$$

where  $f_g = f_{lc} - f_e$  [9]. When the anchoring energy on the surface is assumed to be sufficiently strong, like most liquid crystal cells, the surface term can be neglected therefore, equation (2.15) becomes

$$\begin{aligned} F &= \int (f_{lc} - f_e) dV \\ &= \iiint \left[ \frac{1}{2} K_{11} (\nabla \cdot \bar{n})^2 + \frac{1}{2} K_{22} (\bar{n} \cdot \nabla \times \bar{n} + q_0)^2 + \frac{1}{2} K_{33} (\bar{n} \times \nabla \times \bar{n})^2 \right] dx dy dz \cdot \quad (2.16) \\ &\quad - \iiint \left[ \frac{1}{2} (\epsilon_0 \epsilon_{\perp} (-\nabla v)^2 + \frac{1}{2} \epsilon_0 \Delta \epsilon (\bar{n} \cdot (-\nabla v)^2) \right] dx dy dz. \end{aligned}$$

### 2.1.6 Comparison of the tensor form and vector form

There are two kinds of forms to represent the free energy density of a liquid crystal system. One is the vector form in which the free energy density can be expressed in terms of a vector  $\bar{n}$ , i.e. a director. The other is tensor form in which the free energy density can be expressed in terms of the tensor order parameter  $Q$  [6,8,17]. In the Cartesian vector representation, the discretized free energy representation gives different free energies for  $\bar{n}$  and  $-\bar{n}$ . However, in real nematic phase,  $\bar{n}$  and  $-\bar{n}$  are equivalent and should give the same energy. On the other hand, in the  $Q$  tensor representation, it always incorporates the multiplication of two  $\bar{n}$ 's. This means that the sign of  $\bar{n}$  is always cancelled out. From the mathematical point of view, the tensor form seems to be more appropriate to represent the free energy density of the liquid crystal system. However, the inversion symmetry of the tensor formulation can cause the calculation to give not only inaccurate results, but also physically impossible ones. For example, the tensor form can allow the continuous transformation between splay state and bend state, which are topologically inequivalent states in the pi-cell system [18]. Nevertheless, this is impossible in experiment, because the two states with topologically inequivalent configuration can not be transformed from one to the other without the motion of an isotropic core defect [19]. Though the vector representation cannot preserve the property of inversion symmetry, it is mathematically simpler. When the director does not change steeply, the vector approach is physically correct and reasonable. Moreover, the advantages of the vector form over the tensor form are fewer calculation time, fewer grid points and more reliable. So in this thesis, we use the vector form to represent the free energy density of the liquid crystal system.

## 2.2 Numerical method

Over the recent years, the liquid crystal displays (LCDs) have been widely used for applications such as computer monitors and flat-panel TVs. Nowadays, the size of LCDs becomes more and more large, however, the pixel size becomes smaller and smaller in order to obtain finer resolution and high image quality. As LCDs become so sophisticated, the accurate analysis and design of liquid crystal modes for displays by computer simulation is becoming more and more important. Simulation tools can help us to understand the behavior of the director and optical properties of LCDs. Therefore, the design and the prediction for the performance of LCDs can be completely achieved by using the simulation software without undertaking all steps of the development experimentally.

Simple analysis has been performed in one-dimension to optimize the area in the center of pixels of LCDs [20,21]. This one-dimension means that the director varies only in the Cartesian Z-direction and requires the assumption that the electric-field distribution is uniform in the X-direction and Y-direction. The two-dimensional (2-D) simulation tool provides the more practical results, which considers the director variation and nonuniform fields in the Cartesian X-Z plane by assuming the electric-field distribution to be uniform in the Y direction [22,23]. Although the simple and faster 1-D and 2-D simulation tools are adequate for the modeling of liquid crystal devices, there are some cases where they cannot provide a satisfactory representation for the behavior of devices with complex structures. There are many features occurring in the liquid crystal devices, like multidomain vertically aligned (MVA) and in-plane switching (IPS) LCDs, that are truly three-dimension, hence the 3-D simulation tool is required to optimize and design these devices [17,24,25].



### 2.2.1 Comparison of the finite difference method and finite element method

The finite difference is much more straightforward than the finite element method and for this reason it is the more commonly used approach [8]. In this method, the solution region is divided into a lot of meshes of a regular shape such as rectangles for 2-D modeling or rectangular cubes for 3-D modeling, which have the same dimensions. The derivatives are performed on the “mesh points”, or “grid points” by using the Taylor series expansions shown as follows

$$f(x + \Delta x) = f(x) + f'(x)\Delta x + \frac{f''(x)}{2}(\Delta x)^2 + \frac{f'''(x)}{6}(\Delta x)^3 + \dots \quad (2.17)$$

For example, the forward difference formula can be obtained by solving for the first derivative  $f'(x)$  in equation (2.17):

$$f'(x) = \frac{f(x + \Delta x) - f(x)}{\Delta x} - \frac{f''(x)}{2}\Delta x + \dots \approx \frac{f(x + \Delta x) - f(x)}{\Delta x}. \quad (2.18)$$

Therefore, the governing equations of the system can be discretized as difference equations for the grid points, in other words, the finite difference method gives a “pointwise” approximation to the governing equations of the system. The accuracy of this method depends on the numbers of grid points.

In the finite elements method, the solution region is divided into a finite number of interconnected sections, or elements of a similar shape such as triangle element for 2-D modeling or tetrahedral element for 3-D modeling [26]. The vertices of these elements are called “nodes”. Unlike the finite difference model, the finite element method, gives a “piecewise” approximation to the governing equations of the system.

The detail procedures are well described in section 2.2.2. The basic premise of the finite element method is that a solution region can be approximated by replacing it with an assemblage of discrete elements. Since these elements can be put together in a variety of ways, they can be used to represent the solution region with complex shapes. The accuracy of this method depends not only on the size and number of the elements but also on the interpolation function which is used to approximate the distribution of the field variable within an element.

An advantage of the finite element method over the finite difference method is that the boundary conditions of the problem are easily handled. Many physical problems have boundary conditions involving derivatives and irregular shaped boundaries. The boundary condition of this type is difficult to handle by using the finite difference method, since the irregular shape of the boundary makes placing the grid points difficult. However, the finite element method includes the boundary conditions as integrals in a functional that is being minimized. Therefore, the construction procedure is independent of the particular boundary conditions of the problem. This comparison is not intended to suggest that the finite element method is better than the finite difference method for all problems. Here, we only demonstrate that the finite element method is particularly well suited for problems with complex geometries.

Nowadays, the liquid crystal devices involve the complex patterned electrode structures due to the needs of wide viewing angle, such as multidomain MVA and IPS as wells as multidomain TN and STN modes. Thus, the finite element method is more suited for modeling the simulation tool to accurately predict the behavior of liquid crystal molecules near the irregular boundaries. In this thesis, we will show how the finite element method is implemented for simulating the liquid crystal devices.

### **2.2.2 Three-dimensional modeling using the finite element method**

In the continuum problem, the field variables possess infinite values because they are functions of each generic point in the solution region. Consequently, the problem becomes one with an infinite number of unknowns. The finite element method reduces the problem to one with finite unknowns by dividing the solution region into elements and by expressing the unknown field variable in terms of an interpolation function within each element. The interpolation functions (sometimes called shape functions) are defined in terms of the values of field variables at nodes. The nodal values of the field variables and the interpolation functions completely define the behavior of the field variables within the elements. For the finite element representation of a problem, the nodal values of the field variables become the unknowns. Once the unknowns are found, the interpolation functions define the distribution of field variables through the assemblage of elements. The most important feature of the finite element method over other numerical methods is its ability to formulate solutions for individual elements before putting them together to represent the entire problem. Moreover, there are several methods to formulate the properties of individual elements. To summarize how the finite element method is implemented in the modeling of liquid crystal devices, we simply list these steps as follows. In this modeling, the liquid crystal system with an application of external electric source is considered therefore, the director field and the electric potential become the field variables of the problem.

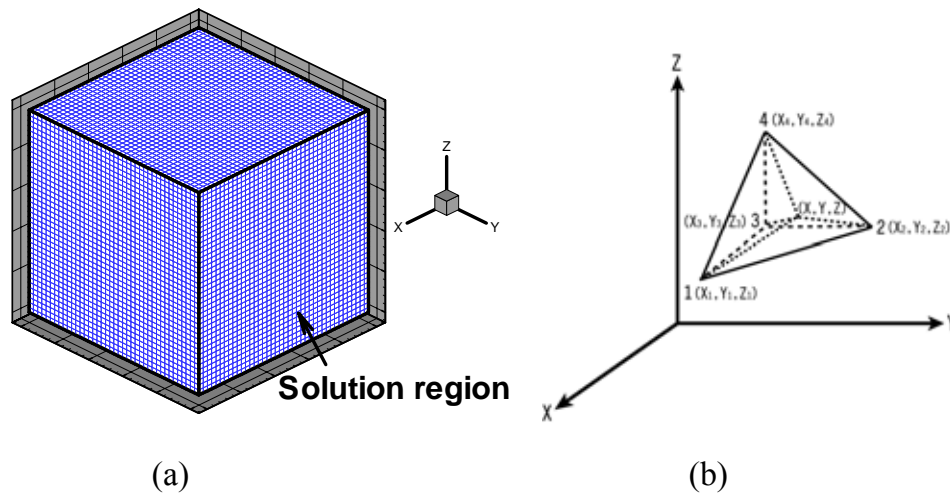


Figure 2.3 (a) A rectangular cubic solution region for the three-dimensional modeling of the liquid crystal system. (b) A tetrahedral element whose nodes are numbered according to the right-hand rule. The point  $(x,y,z)$  is some point within the element.

**1. Select the element shape and discretize the solution region.** In the three-dimensional modeling of the liquid crystal system, the computational region with the rectangular cubic shape, as shown in Fig. 2.3(a), is selected as our solution region. Here, the four-node tetrahedral element, as shown in Fig. 2.3(b), is selected to divide the solution region. The nodes are numbered in the right-handed Cartesian coordinate system and nodes 1, 2, and 3 are counterclockwise ordered when viewed from node 4.

**2. Select the interpolation functions.** In this step, the nodal values of the director field  $\bar{n}(x,y,z)$  and electric potential  $v(x,y,z)$  are assigned, respectively at each node of each element, as shown in Fig. 2.4. However, the magnitudes of nodal values are assumed to be unknowns in the problem. Under the assumption of continuum theory, we assume the director field and electric potential to vary linearly over each element.

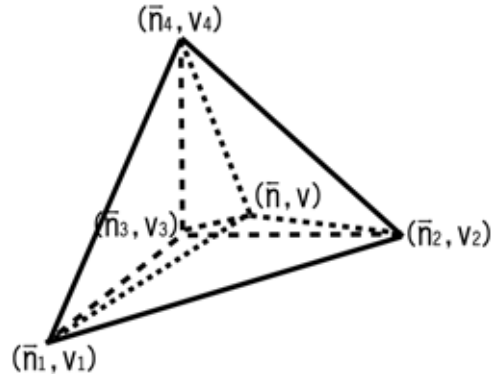


Figure 2.4 The nodal values of the director field and electric potential are assigned, respectively at each node of the tetrahedral element.  $\bar{n}$  and  $v$  are the approximation values of the director field and electric potential, respectively at some point within the element.

Therefore, the polynomials, as shown in equations (2.19) and (2.20), are selected to represent the distribution of the director field and electric potential, respectively within the element (e):

$$\bar{n}^e(x, y, z) = a^e + b^e x + c^e y + d^e z, \quad (2.19)$$

$$v^e(x, y, z) = a^e + b^e x + c^e y + d^e z, \quad (2.20)$$

where  $a^e$ ,  $b^e$ ,  $c^e$  and  $d^e$  are constants to be determined and the degree of the polynomial depends on the number of nodes assigned to the element. Equation (2.19) and equation (2.20) state that the director field and electric potential vary linearly within the element and along the element boundaries. Such behaviors of polynomials ensure the continuity of the director field and electric potential throughout all elements in solution region. After defining the director field and electric potential within an element, we are now ready to find the constants in terms of coordinates and nodal values of nodes.

Evaluating equation (2.19) at each node gives a set of equations:

$$\begin{aligned}
 \text{For node 1} \quad \bar{n}_1^e &= a_1^e + b_1^e x_1 + c_1^e y_1 + d_1^e z_1 \\
 \text{For node 2} \quad \bar{n}_2^e &= a_1^e + b_1^e x_2 + c_1^e y_2 + d_1^e z_2 \\
 \text{For node 3} \quad \bar{n}_3^e &= a_1^e + b_1^e x_3 + c_1^e y_3 + d_1^e z_3 \\
 \text{For node 4} \quad \bar{n}_4^e &= a_1^e + b_1^e x_4 + c_1^e y_4 + d_1^e z_4
 \end{aligned} \tag{2.21}$$

Similarly, for the electric potential, we have

$$\begin{aligned}
 \text{For node 1} \quad v_1^e &= a_2^e + b_2^e x_1 + c_2^e y_1 + d_2^e z_1 \\
 \text{For node 2} \quad v_2^e &= a_2^e + b_2^e x_2 + c_2^e y_2 + d_2^e z_2 \\
 \text{For node 3} \quad v_3^e &= a_2^e + b_2^e x_3 + c_2^e y_3 + d_2^e z_3 \\
 \text{For node 4} \quad v_4^e &= a_2^e + b_2^e x_4 + c_2^e y_4 + d_2^e z_4
 \end{aligned} \tag{2.22}$$

with a little algebraic manipulation we can solve equation (2.21) for constants  $a_1^e, b_1^e, c_1^e$  and  $d_1^e$  in terms of nodal values,  $\bar{n}_i^e$ ,  $i=1\sim 4$  and nodal coordinates  $(x_i, y_i, z_i)$ ,  $i=1\sim 4$ . Substituting these constants into equation (2.19), we obtain

$$\bar{n}^e(x, y, z) = \frac{\begin{vmatrix} 1 & x & y & z \\ 1 & x_2 & y_2 & z_2 \\ 1 & x_3 & y_3 & z_3 \\ 1 & x_4 & y_4 & z_4 \end{vmatrix}}{6V} \bar{n}_1^e + \frac{\begin{vmatrix} 1 & x_1 & y_1 & z_1 \\ 1 & x & y & z \\ 1 & x_3 & y_3 & z_3 \\ 1 & x_4 & y_4 & z_4 \end{vmatrix}}{6V} \bar{n}_2^e$$

$$+ \frac{\begin{vmatrix} 1 & x_1 & y_1 & z_1 \\ 1 & x_2 & y_2 & z_2 \\ 1 & x & y & z \\ 1 & x_4 & y_4 & z_4 \end{vmatrix}}{6V} \bar{n}_3^e + \frac{\begin{vmatrix} 1 & x_1 & y_1 & z_1 \\ 1 & x_2 & y_2 & z_2 \\ 1 & x_3 & y_3 & z_3 \\ 1 & x & y & z \end{vmatrix}}{6V} \bar{n}_4^e,$$
(2.23)

where

$$6V = \begin{vmatrix} 1 & x_1 & y_1 & z_1 \\ 1 & x_2 & y_2 & z_2 \\ 1 & x_3 & y_3 & z_3 \\ 1 & x_4 & y_4 & z_4 \end{vmatrix} = 6 \left( \begin{array}{l} \text{volume of tetrahedral element} \\ \text{defined by nodes 1,2,3,4} \end{array} \right)$$
(2.24)

Following the same procedure for equation (2.22), we finally obtain

$$v^e(x, y, z) = \frac{\begin{vmatrix} 1 & x & y & z \\ 1 & x_2 & y_2 & z_2 \\ 1 & x_3 & y_3 & z_3 \\ 1 & x_4 & y_4 & z_4 \end{vmatrix}}{6V} v_1^e + \frac{\begin{vmatrix} 1 & x_1 & y_1 & z_1 \\ 1 & x & y & z \\ 1 & x_3 & y_3 & z_3 \\ 1 & x_4 & y_4 & z_4 \end{vmatrix}}{6V} v_2^e$$

$$+ \frac{\begin{vmatrix} 1 & x_1 & y_1 & z_1 \\ 1 & x_2 & y_2 & z_2 \\ 1 & x & y & z \\ 1 & x_4 & y_4 & z_4 \end{vmatrix}}{6V} v_3^e + \frac{\begin{vmatrix} 1 & x_1 & y_1 & z_1 \\ 1 & x_2 & y_2 & z_2 \\ 1 & x_3 & y_3 & z_3 \\ 1 & x & y & z \end{vmatrix}}{6V} v_4^e.$$
(2.25)



Now we define

$$S_i^e(x, y, z) = \frac{1}{6V} (A_i + B_i x + C_i y + D_i z), \quad i = 1, 2, 3, 4, \quad (2.26)$$

where

$$A_1 = \begin{vmatrix} x_2 & y_2 & z_2 \\ x_3 & y_3 & z_3 \\ x_4 & y_4 & z_4 \end{vmatrix}, \quad B_1 = - \begin{vmatrix} 1 & y_2 & z_2 \\ 1 & y_3 & z_3 \\ 1 & y_4 & z_4 \end{vmatrix}, \quad C_1 = \begin{vmatrix} 1 & x_2 & z_2 \\ 1 & x_3 & z_3 \\ 1 & x_4 & z_4 \end{vmatrix}, \quad D_1 = - \begin{vmatrix} 1 & x_2 & y_2 \\ 1 & x_3 & y_3 \\ 1 & x_4 & y_4 \end{vmatrix}. \quad (2.27)$$

In general, the functions,  $S_i^e(x, y, z)$ ,  $i=1\sim 4$ , are called interpolation functions or shape functions and they play an important role in the finite element analyses. After defining the shape functions, the equations (2.23) and (2.25) can be rewritten, respectively as

$$\begin{aligned} \bar{n}^e(x, y, z) &= S_1^e(x, y, z)\bar{n}_1^e + S_2^e(x, y, z)\bar{n}_2^e + S_3^e(x, y, z)\bar{n}_3^e + S_4^e(x, y, z)\bar{n}_4^e \\ &= \sum_{i=1}^4 S_i^e(x, y, z)\bar{n}_i^e, \end{aligned} \quad (2.28)$$

and

$$\begin{aligned} v^e(x, y, z) &= S_1^e(x, y, z)v_1^e + S_2^e(x, y, z)v_2^e + S_3^e(x, y, z)v_3^e + S_4^e(x, y, z)v_4^e \\ &= \sum_{i=1}^4 S_i^e(x, y, z)v_i^e. \end{aligned} \quad (2.29)$$

It we let

$$\{\bar{\mathbf{n}}^e\} = \begin{Bmatrix} \bar{\mathbf{n}}_1^e \\ \bar{\mathbf{n}}_2^e \\ \bar{\mathbf{n}}_3^e \\ \bar{\mathbf{n}}_4^e \end{Bmatrix}, \quad \{\mathbf{v}^e\} = \begin{Bmatrix} \mathbf{v}_1^e \\ \mathbf{v}_2^e \\ \mathbf{v}_3^e \\ \mathbf{v}_4^e \end{Bmatrix},$$

and

$$[\mathbf{S}^e(x, y, z)] = [\mathbf{S}_1^e(x, y, z), \mathbf{S}_2^e(x, y, z), \mathbf{S}_3^e(x, y, z), \mathbf{S}_4^e(x, y, z)].$$

By using the matrix notation, equations (2.28) and (2.29) can be rewritten as

$$\bar{\mathbf{n}}^e(x, y, z) = [\mathbf{S}^e(x, y, z)] \{\bar{\mathbf{n}}^e\}, \quad (2.30)$$

$$\mathbf{v}^e(x, y, z) = [\mathbf{S}^e(x, y, z)] \{\mathbf{v}^e\}. \quad (2.31)$$

If the solution region contains  $M$  elements, the complete representation of the director field and electric potential over the whole region are given by

$$\bar{\mathbf{n}}(x, y, z) = \sum_{e=1}^M \bar{\mathbf{n}}^e(x, y, z) = \sum_{e=1}^M [\mathbf{S}^e(x, y, z)] \{\bar{\mathbf{n}}^e\}, \quad (2.32)$$

$$\mathbf{v}(x, y, z) = \sum_{e=1}^M \mathbf{v}^e(x, y, z) = \sum_{e=1}^M [\mathbf{S}^e(x, y, z)] \{\mathbf{v}^e\}. \quad (2.33)$$

From equations (2.32) and (2.33), we know that if the nodal values of the director field and electric potential are known, the complete solution region can be obtained by interconnecting the solution region of the tetrahedral element. This is the so-called “piecewise” approximation.

**3. Find the element equations.** Once the shape and shape function of the element have been selected, we are ready to determine the element equations which express the properties of the individual element. For this task, the variational method is used. In order to make the liquid crystal system stationary, we require that

$$\delta F(\bar{n}, v) = \frac{\partial F}{\partial \bar{n}} \delta \bar{n} + \frac{\partial F}{\partial v} \delta v = 0, \quad (2.34)$$

where  $F(\bar{n}, v)$  is the total free energy of the liquid crystal system obtained from equation (2.16). Since  $\delta \bar{n}$  and  $\delta v$  are independent, equation (2.34) can hold only if

$$\frac{\partial F}{\partial \bar{n}} = \frac{\partial F}{\partial v} = 0. \quad (2.35)$$

If the shape functions of the director field and electric potential obey certain continuity and compatibility conditions, then the functional  $F(\bar{n}, v)$  can be written as a sum of individual functionals defined for all elements of the assemblage, that is,

$$F(\bar{n}, v) = \sum_{e=1}^M F^e(\bar{n}^e, v^e), \quad (2.36)$$

where  $M$  is the total number of elements and superscript (e) denotes an element. Therefore, instead of working with the functional defined over the whole solution region, we may focus our attention on the functional for the individual element.

From equations (2.34) and (2.36), we have

$$\delta F(\bar{\mathbf{n}}, \mathbf{v}) = \sum_{e=1}^M \delta F^e(\bar{\mathbf{n}}^e, \mathbf{v}^e) = 0. \quad (2.37)$$

Equation (2.37) implies that

$$\frac{\partial F^e}{\partial \bar{\mathbf{n}}^e} = \frac{\partial F^e}{\partial \mathbf{v}^e} = 0. \quad (2.38)$$

From equations (2.28) and (2.29), we obtain

$$\frac{\partial F^e}{\partial \bar{n}_i^e} = \frac{\partial F^e}{\partial v_i^e} = 0, \quad i = 1, 2, \dots, r, \quad (2.39)$$

where  $r$  is the number of nodes assigned to the element ( $e$ ) and the variation of  $F^e(\bar{\mathbf{n}}^e, \mathbf{v}^e)$  is taken only with respect to the nodal values associated with the element. Equation (2.39) comprises a set of  $2r$  equations that characterizes the behavior of the element ( $e$ ). The fact that we can present the functional for the assemblage of all elements as the sum of functionals for all individual elements provides the key to formulating individual element equations from a variation method.

In the liquid crystal modeling, the functional of an element is given by equation (2.16) and from the relationship:

$$(\bar{\mathbf{n}} \cdot \nabla \times \bar{\mathbf{n}})^2 + (\bar{\mathbf{n}} \times \nabla \times \bar{\mathbf{n}})^2 = (\nabla \times \bar{\mathbf{n}})^2, \quad (2.40)$$

and the constraint condition for director, we can rewrite the functional as

$$\begin{aligned} & \tilde{F}^e(\bar{\mathbf{n}}^e, \mathbf{v}^e) \\ &= \iiint \left\{ \frac{1}{2} K_{11} (\nabla \cdot \bar{\mathbf{n}}^e)^2 + \frac{1}{2} (K_{22} - K_{33}) (\bar{\mathbf{n}}^e \cdot \nabla \times \bar{\mathbf{n}}^e)^2 + \frac{1}{2} K_{33} (\nabla \times \bar{\mathbf{n}}^e)^2 \right. \\ &+ K_{22} q_0 (\bar{\mathbf{n}}^e \cdot \nabla \times \bar{\mathbf{n}}^e) - \frac{1}{2} [\varepsilon_0 \varepsilon_{\perp} (-\nabla v^e)^2 + \varepsilon_0 \Delta \varepsilon (\bar{\mathbf{n}}^e \cdot (-\nabla v^e)^2)] \left. \right\} dx dy dz \quad (2.41) \\ &- \iiint \left[ \frac{1}{2} \Gamma (\bar{\mathbf{n}}^e \cdot \bar{\mathbf{n}}^e) \right] dx dy dz \\ &= F^e(\bar{\mathbf{n}}^e, \mathbf{v}^e) - \Gamma G(\bar{\mathbf{n}}^e), \end{aligned}$$

where the constant term is dropped and a Lagrange multiplier  $\Gamma$  is used to maintain the unit length of the director. Substitution of equations (2.28) and (2.29) into equation (2.41), we have

$$\tilde{F}^e(\bar{\mathbf{n}}, \mathbf{v}) = \tilde{F}^e\left(\sum_{i=1}^4 S_i \bar{\mathbf{n}}_i, \sum_{i=1}^4 S_i \mathbf{v}_i\right) = \tilde{F}^e(\bar{\mathbf{n}}_i, \mathbf{v}_i), \quad i = 1, 2, 3, 4, \quad (2.42)$$

and

$$\begin{aligned} \nabla \cdot \bar{\mathbf{n}} &= \sum_{i=1}^4 [\nabla S_i] \cdot \bar{\mathbf{n}}_i \equiv \sum_{i=1}^4 \bar{\mathbf{m}}_i \cdot \bar{\mathbf{n}}_i, \\ \nabla \times \bar{\mathbf{n}} &= \sum_{i=1}^4 [\nabla S_i] \times \bar{\mathbf{n}}_i \equiv \sum_{i=1}^4 \bar{\mathbf{m}}_i \times \bar{\mathbf{n}}_i, \\ \nabla v &= \sum_{i=1}^4 [\nabla S_i] v_i \equiv \sum_{i=1}^4 \bar{\mathbf{m}}_i v_i, \end{aligned} \quad (2.43)$$

where

$$\bar{\mathbf{m}}_1 = \left( \frac{-1}{6V} \right) \left( \begin{array}{c} \left| \begin{array}{ccc} 1 & y_2 & z_2 \\ 1 & y_3 & z_3 \\ 1 & y_4 & z_4 \end{array} \right|, & - \left| \begin{array}{ccc} 1 & x_2 & z_2 \\ 1 & x_3 & z_3 \\ 1 & x_4 & z_4 \end{array} \right|, & \left| \begin{array}{ccc} 1 & x_2 & y_2 \\ 1 & x_3 & y_3 \\ 1 & x_4 & y_4 \end{array} \right| \end{array} \right)$$

$$\bar{\mathbf{m}}_2 = \left( \frac{1}{6V} \right) \left( \begin{array}{c} \left| \begin{array}{ccc} 1 & y_1 & z_1 \\ 1 & y_3 & z_3 \\ 1 & y_4 & z_4 \end{array} \right|, & - \left| \begin{array}{ccc} 1 & x_1 & z_1 \\ 1 & x_3 & z_3 \\ 1 & x_4 & z_4 \end{array} \right|, & \left| \begin{array}{ccc} 1 & x_1 & y_1 \\ 1 & x_3 & y_3 \\ 1 & x_4 & y_4 \end{array} \right| \end{array} \right)$$

$$\bar{\mathbf{m}}_3 = \left( \frac{-1}{6V} \right) \left( \begin{array}{c} \left| \begin{array}{ccc} 1 & y_1 & z_1 \\ 1 & y_2 & z_2 \\ 1 & y_4 & z_4 \end{array} \right|, & - \left| \begin{array}{ccc} 1 & x_1 & z_1 \\ 1 & x_2 & z_2 \\ 1 & x_4 & z_4 \end{array} \right|, & \left| \begin{array}{ccc} 1 & x_1 & y_1 \\ 1 & x_2 & y_2 \\ 1 & x_4 & y_4 \end{array} \right| \end{array} \right)$$

$$\bar{\mathbf{m}}_4 = \left( \frac{1}{6V} \right) \left( \begin{array}{c} \left| \begin{array}{ccc} 1 & y_1 & z_1 \\ 1 & y_2 & z_2 \\ 1 & y_3 & z_3 \end{array} \right|, & - \left| \begin{array}{ccc} 1 & x_1 & z_1 \\ 1 & x_2 & z_2 \\ 1 & x_3 & z_3 \end{array} \right|, & \left| \begin{array}{ccc} 1 & x_1 & y_1 \\ 1 & x_2 & y_2 \\ 1 & x_3 & y_3 \end{array} \right| \end{array} \right).$$

Hence the functional of the element can be expressed in terms of the nodal values of the director field and electric potential and the element equations can be obtained by substituting equation (2.42) into equation (2.39). However, because the nodal value of the director field is a vector, that is,  $\bar{\mathbf{n}} = (n_x, n_y, n_z)$ , the variation in equation (2.39) has to be taken for the components of a director, respectively so that we have

$$\frac{\partial \tilde{\mathbf{F}}^e}{\partial \bar{\mathbf{n}}_i^e} = \frac{\partial \tilde{\mathbf{F}}^e}{\partial n_{ij}^e} = 0 \quad i = 1, 2, 3, 4; \quad j = x, y, z, \quad (2.44)$$

$$\frac{\partial \tilde{\mathbf{F}}^e}{\partial v_i^e} = 0 \quad i = 1, 2, 3, 4. \quad (2.45)$$

For a dynamic solution, that is, the nodal unknowns are a function of time we have to derive the dynamic equations for director. In this stage, we add a Rayleigh dissipation function to the element equations (2.44), therefore the equation of motion for director in an element can be expressed by

$$\frac{\partial \tilde{F}^e}{\partial \mathbf{n}_{ij}^e} + \frac{\partial F_d^e}{\partial \dot{\mathbf{n}}_{ij}^e} = 0 \quad i = 1,2,3,4; \quad j = x, y, z. \quad (2.46)$$

The dissipation function takes the form [21]:

$$F_d^e = \iiint \frac{1}{2} \gamma_1 (\dot{n}_x^2 + \dot{n}_y^2 + \dot{n}_z^2) dx dy dz, \quad (2.47)$$

where  $\gamma_1$  is the rotational viscosity of liquid crystals. However, it is impossible to simultaneously solve equation (2.46) for director component and Lagrange multiplier  $\Gamma$ . Therefore, we drop the Lagrange multiplier term and renormalize the director to be of unit length after each iteration. Under this condition, equation (2.46) can be rewritten as

$$\frac{\partial F^e}{\partial \mathbf{n}_{ij}^e} + \frac{\partial F_d^e}{\partial \dot{\mathbf{n}}_{ij}^e} = 0 \quad i = 1,2,3,4; \quad j = x, y, z. \quad (2.48)$$

On the other hand, equation (2.45) can be rewritten as

$$\frac{\partial F_e^e}{\partial \mathbf{v}_i^e} = 0 \quad i = 1,2,3,4, \quad (2.49)$$

where the  $F_e^e$  is the electric free energy obtained by integrating equation (2.11) over the element volume.

**4. Assemble the element equations to obtain the system equation.** To find the properties of the overall liquid crystal system modeled by the network of elements, we must assemble all element properties. The complete set of system equations for the liquid crystal system is assembled by adding the element equation shown in equation (2.48) and (2.49), respectively, that is,

$$\text{For director field } \frac{\partial F}{\partial \mathbf{n}_{ij}} + \frac{\partial F_d}{\partial \dot{\mathbf{n}}_{ij}} = \sum_{e=1}^M \left( \frac{\partial F^e}{\partial \mathbf{n}_{ij}^e} + \frac{\partial F_d^e}{\partial \dot{\mathbf{n}}_{ij}^e} \right) = 0 \quad i = 1, 2, \dots, N; j = x, y, z, \quad (2.50)$$

$$\text{For electric potential } \frac{\partial F}{\partial v_i} = \sum_{e=1}^M \frac{\partial F_e^e}{\partial v_i} = 0 \quad i = 1, 2, \dots, N, \quad (2.51)$$

where  $N$  is the total node numbers of the system. Note that for some global node  $i$  in equations (2.50) and (2.51), only elements sharing node the  $i$  will contribute to the variations of  $\partial F/\partial \mathbf{n}_{ij} + \partial F_d/\partial \dot{\mathbf{n}}_{ij}$  and  $\partial F/\partial v_i$ . The problem is solved when a set of  $3N$  equations from equation (2.50) and a set of  $N$  equations from equation (2.51) are simultaneously solved for the  $N$  nodal vector values of the director field and  $N$  nodal scalar values of electric potential. However, these simultaneous equations are hardly to solve so that we derive the update formula for director field and electric potential. By using the forward difference approximation shown in equation (2.18) for the time derivative in equation (2.50), we obtain the update formula for director as

$$\begin{aligned} \sum_{e=1}^M \frac{\partial F^e}{\partial \mathbf{n}_{ij}^e} &= - \sum_{e=1}^M \frac{\partial F_d^e}{\partial \dot{\mathbf{n}}_{ij}^e} = -6\gamma_1 \dot{\mathbf{n}}_{ij} = -6\gamma_1 \frac{\mathbf{n}_{ij}^{\text{new}} - \mathbf{n}_{ij}^{\text{old}}}{\Delta t} \\ \Rightarrow \mathbf{n}_{ij}^{\text{new}} &= \mathbf{n}_{ij}^{\text{old}} - \frac{\Delta t}{6\gamma_1} \sum_{e=1}^M \frac{\partial F^e}{\partial \mathbf{n}_{ij}^e} \quad i = 1, 2, \dots, N; j = x, y, z, \end{aligned} \quad (2.52)$$



here the time derivatives for the director components in an element are assumed to be the same. If the solution region is finely cut, this assumption is reasonable. On the other hand, when equation (2.51) is discretized, a linear equation for the discretized nodal voltage is derived. This equation can be directly solved for the voltage at the current node in terms of the voltage and the directors at the surrounding nodes as shown in equation (2.53):

$$v_i^{\text{new}} = -\sum_{e=1}^M f^e(v_j^{\text{old}}, \bar{n}) \quad i = 1, 2, \dots, N; \quad i \neq j, \quad (2.53)$$

where  $f^e(v_j^{\text{old}}, \bar{n})$  is the function of nodal voltage and director at surrounding nodes in an element containing the global node.

**5. Impose the initial conditions and boundary conditions.** Before the update equations in equations (2.52) and (2.53) are ready for iteration, the initial conditions for director and voltage must be given first. The initial conditions are very impotent to the accuracy and speed of the calculation. For the calculations of dynamics of a liquid crystal system, the initial director field should be the desired state form which the dynamics begins and the initial voltage distribution can be lineally given along the normal direction of the cell. For the boundary conditions, the periodic boundary conditions in the X and Y directions are taken in our modeling. Dirichlet boundary conditions are assumed for the  $Z = 0$  and  $Z = d$  planes corresponding to strong anchoring. That means the known nodal values of director field and electric potential must to be imposed on the surface layer.

**6. Solve the system equations.** The assembly process gives a set of simultaneous equations that we solve to obtain the unknown nodal directors and electric potential. For the director field, because equation (2.50) is a set of nonlinear equations for

director components, it can be solved by the relaxation method which is stable and gives acceptable convergence. Once the initial director and voltage distribution are given, the solution of director distribution can be obtained by iterating the update formula (2.52). However, as stated previously, this update formula does not maintain the unit length of the director. Therefore, after the director is updated, each node director must be renormalized to have the unit length by using equation (2.54) after each iteration.

$$n_{ij} = \frac{n_{ij}}{\sqrt{(n_{ix}^2 + n_{iy}^2 + n_{iz}^2)}} \quad i = 1, 2, \dots, N; j = x, y, z. \quad (2.54)$$

For the electric potential, because equation (2.51) is a set of linear equations for the nodal voltage, it can be directly solved from the update formula (2.53) when the director field is given. Because the voltage distribution is dependent on the director field, in other words, the voltage distribution changes with the variation of the director field. Hence, we need to solve iteratively the system equations for director field and voltage distribution in turn until the equilibrium state is reached. On the other hand, for the calculations of dynamics of liquid crystal system, the new director configuration and new voltage distribution must be calculated, respectively before any nodal variables are updated. After the new director configuration and voltage distribution are calculated for each time step, the old director configuration and voltage distribution are updated by the new ones. This is called “simultaneously displacement” when all nodal variables are updated simultaneously. When the above procedure is completed, we increase the time step  $\Delta t$  and repeat the same updating procedure until the equilibrium state is reached. Figure 2.5 illustrates the simplified flow chart of the program.

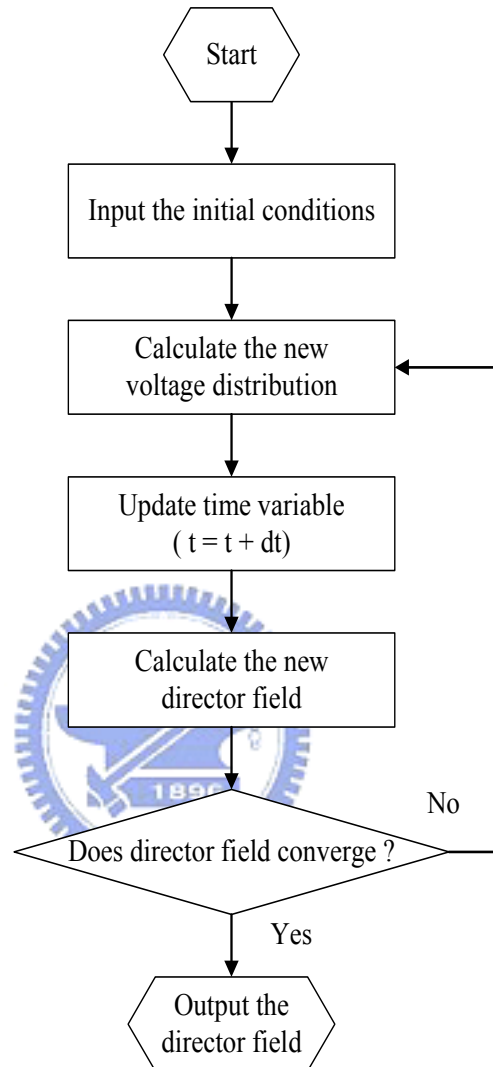


Figure 2.5 The simplified flow chart of the program for calculating the director field and voltage distribution of the liquid crystals.

## References

- [1] E. C. Gartland, Jr., P. Palffy-Muhoray and R. S. Varga: “Numerical minimization of the Landau-de Gennes free energy: defects in cylindrical capillaries” *Mol. Cryst. Liq. Cryst.* **199** 429 (1991).
- [2] C. W. Oseen: “The theory of liquid crystals” *Trans. Faraday Soc.* **29** 883 (1933).
- [3] H. Zocher: *Trans. Faraday Soc.* **28** 945 (1933).
- [4] F. C. Frank: “Liquid crystals: On the theory of liquid crystals” *Disc. Faraday Soc.* **25** 19 (1958).
- [5] J. L. Ericksen: “Hydrostatic theory of liquid crystals” *Arch. Rational Mech. Anal.* **10** 189 (1962).
- [6] P. G. de Gennes and J. Prost: *The Physics of Liquid Crystals* (Clarendon Press, Oxford, 1993) 2nd ed.
- [7] D. J. Griffiths: *Introduction to Electrodynamics* (Prentice Hall, New Jersey, 1989) 2nd ed. chap. 4.
- [8] J. E. Anderson, P. E. Watson and P. J. Bos: *LC3D Liquid Crystal Display 3-D Director Simulator Software and Technology Guide* (Artech House, Boston, 2001).
- [9] R. N. Thurston and D. W. Berreman: “Equilibrium and stability of liquid-crystal configurations in an electric field” *J. Appl. Phys.* **52** 508 (1981).
- [10] H. B. Callen: *Thermodynamics and an Introduction to Thermostatistics* (Wiley, New York, 1985) 2nd ed.
- [11] A. Rapini and M. Papoular: *J. Phys.* **30** C4-54 (1969).
- [12] *DIMOS User’s Guide* (autronic-MELCHERS GmbH, 1996-2001).

- [13] K. H. Yang: “Freedericksz transition of twisted nematic cells” *Appl. Phys. Lett.* **43** 171 (1983).
- [14] A. Sugimura and G. R. Luckhurst: “Director deformation of a twisted chiral nematic liquid crystal cell with weak anchoring boundaries” *Phys. Rev. E* **52** 681 (1995).
- [15] W. Zhao, C.-X. Wu and M. Iwamoto: “Analysis of weak-anchoring effect in nematic liquid crystals” *Phys. Rev. E* **62** R1481 (2000).
- [16] O. K. C. Tsui, F. K. Lee, B. Zhang and P. Sheng: “First-order liquid crystal orientation transition on inhomogeneous substrates” *Phys. Rev. E* **69** 021704 (2004).
- [17] H. Mori, E. C. Gartland, Jr., J. R. Kelly and P. J. Bos: “Multidimensional director modeling using the Q tensor representation in a liquid crystal cell and its application to the  $\pi$  cell with patterned electrodes” *Jpn. J. Appl. Phys.* **38** 135 (1999).
- [18] J. E. Anderson, P. Watson and P. J. Bos: “Comparisons of the vector method and tensor method for simulating liquid crystal devices” *Liq. Cryst.* **28** 109 (2001).
- [19] H. Nakamura and M. Noguchi: “Bend transition in pi-cell” *Jpn. J. Appl. Phys.* **39** 6368 (2000).
- [20] D. W. Berreman: “Dynamics of liquid-crystal twist cells” *Appl. Phys. Lett.* **25** 12 (1974).
- [21] D. W. Berreman: “Numerical modeling of twisted nematic devices” *Philos. Trans. R. Soc. London Ser. A* **309** 203 (1983).

- [22] J. B. Davies, S. Day, F. D. Pasquale and F. A. Fernandez: “Finite-element modelling in 2-D of nematic liquid crystal structures” *Electron. Lett.* **32** 582 (1996).
- [23] H.-C. Huang, D.-D. Huang and Jun Chen: “Two-dimensional optical analysis of small pixels in reflective silicon microdisplay” *Jpn. J. Appl. Phys.* **39** 485 (2000).
- [24] I. A. Yao, J. J. Wu and S. H. Chen: “Three-dimensional simulation of the homeotropic to planar transition in cholesteric liquid crystals using the finite elements method” *Jpn. J. Appl. Phys.* **43** 705 (2004).
- [25] A. Lien: “Simulation of three-dimensional director structures in twisted nematic liquid crystal displays” *Appl. Phys. Lett.* **62** 1079 (1993).
- [26] W. B. Bickford: *A First Course in the Finite Element Method* (Homewood, Boston, 1990).



# Chapter 3

## Transition between Homeotropic Texture and Planar Texture

### 3.1 Introduction

Bistable reflective display technology is of considerable interest because of its low power consumption and high brightness, high contrast at wide viewing angles, and low manufacturing cost [1,2]. Cholesteric reflective displays have two stable states at zero field [2]. One is the planar texture in which the helical axis is perpendicular to the cell surfaces. The other is the focal-conic texture in which the helical axis is more or less parallel to the cell surfaces [3]. Switching from the focal-conic texture to the planar texture requires the application of a high electric field which forces the liquid crystal system into a homeotropic texture [4]. On removal of the field, a transition from homeotropic texture to planar texture takes place in two steps: homeotropic texture to transient planar texture with the effective pitch  $P^* = (K_{33} / K_{22})P_0$ , and transient planar texture to planar texture with intrinsic pitch  $P_0$  [5-7].

However, the homeotropic-planar texture transition is usually slow [5]. Because of this slow transition, the application of cholesteric liquid crystals is limited to displaying static images. In order to obtain superior cholesteric reflective displays

and a design of driving schemes, we have investigated the dynamics of such a system and show a transformation between textures. On the basis of our simulation results, we suggest methods for improving the response characteristics.

### 3.2 Numerical modeling

In this section, a computer modeling method for three-dimensional dynamic analyses of liquid crystal cells using the finite element method is presented. The details of the numerical method are stated in section 2.2.2. The numerical method is based on a variational approach to the Frank-Oseen free energy formulation and uses a vectorial representation of the director [4]. The modeling employs finite element method for the calculations of director configurations and voltage distribution while uses finite difference method in the time stepping process.

The expression for elastic free energy  $F_{lc}$  of a cholesteric liquid crystal system in terms of the director  $\vec{n}$  is given by

$$F_{lc} = \frac{1}{2} \iiint [K_{11}(\nabla \cdot \vec{n})^2 + K_{22}(\vec{n} \cdot \nabla \times \vec{n})^2 + K_{33}(\vec{n} \times \nabla \times \vec{n})^2 + 2K_{22}q_0(\vec{n} \cdot \nabla \times \vec{n})] dx dy dz, \quad (3.1)$$

where  $K_{11}$ ,  $K_{22}$ ,  $K_{33}$  are elastic constants for splay, twist and bend deformations, respectively.  $q_0 = (2\pi/P_0)$  is the chiral parameter. The expression for electric free energy  $F_e$  of a liquid crystal system in terms of voltage  $v$  is given by

$$F_e = \frac{1}{2} \iiint [\epsilon_0 \epsilon_{\perp} (-\nabla v)^2 + \epsilon_0 \Delta \epsilon (\vec{n} \cdot (-\nabla v))^2] dx dy dz, \quad (3.2)$$



where the dielectric anisotropy  $\Delta\varepsilon = \varepsilon_{\parallel} - \varepsilon_{\perp}$ , and  $\varepsilon_{\parallel}$ ,  $\varepsilon_{\perp}$  are the parallel and perpendicular permittivities of a director relative to the electric field.

Based on the finite element method, the director and voltage within an element can be expressed in terms of the nodal director and nodal voltage, respectively, as well as the interpolation function, therefore, we have

$$\begin{aligned}\bar{\mathbf{n}} &= \sum_{i=1}^4 S_i(x, y, z) \bar{\mathbf{n}}^i, \\ \mathbf{v} &= \sum_{i=1}^4 S_i(x, y, z) v^i.\end{aligned}\quad (3.3)$$

Here  $S_i(x, y, z)$  is the interpolation function,  $\bar{\mathbf{n}}^i$  is the nodal director at node  $i$  and  $v^i$  is the nodal voltage at node  $i$ . By substitution of eq. (3.3) into eqs. (3.1) and (3.2), the Gibbs free energy in eq. (3.4) for one element can be expressed in terms of the nodal director and nodal voltage of the element.

$$F_g = F_{lc} - F_e. \quad (3.4)$$

Ignoring the flow of the director, the dynamic equation of the director becomes a nonlinear equation for nodal director component as expressed by [8,9]

$$\frac{\partial F_g}{\partial \mathbf{n}_\delta^p} - \frac{\partial}{\partial \mathbf{n}_\delta^p} \left( \frac{\Gamma}{2} \iiint \mathbf{n}_\mu^p \mathbf{n}_\mu^p dx dy dz \right) + \frac{\partial}{\partial \dot{\mathbf{n}}_\delta^p} \left( \frac{\gamma_1}{2} \iiint \dot{\mathbf{n}}_\mu^p \dot{\mathbf{n}}_\mu^p dx dy dz \right) = 0, \quad (3.5)$$

where the Lagrange multiplier  $\Gamma$  is used to maintain the unit length of the director. However, one cannot simultaneously solve this equation for  $\Gamma$  and  $\bar{\mathbf{n}}$ . Therefore, the  $\Gamma$  term is dropped and  $\bar{\mathbf{n}}$  is renormalized to have a unit length after each time step

[6,10]. In each element, for  $\delta = x, y$  or  $z$ ,  $p = 1, 2, 3$  or  $4$ , and  $\mu (=x, y$  and  $z)$  implies summation, where  $\gamma_1$  is the rotational viscosity of a liquid crystal material. After using the forward difference approximation for time derivative, we can obtain the numerical update equation for director at each node in terms of the directors and voltage at that and surrounding nodes. Given the initial conditions for director and voltage, this update equation for nodal director can be solved by the relaxation method which is stable and gives acceptable convergence.

Because the dielectric constant is anisotropic, the voltage at each node depends on the directors at that and surrounding nodes. After solving Maxwell's equation in equation (3.6), an equation linear in nodal voltage is derived as

$$\nabla \cdot \vec{D} = 0, \quad (3.6)$$

where  $\vec{D}$  is the electric displacement. Given a director configuration, this equation can be rewritten as a numerical update equation for voltage at current node in terms of the neighboring nodal voltage and it can be solved by using the successive over-relaxation method which is similar to the relaxation method but gives faster convergence [10].

In order to calculate the dynamics of the system, the new director configuration must be calculated before any variables are updated. When the old director configuration is updated by the new director configuration after each time step, the voltage distribution can be calculated directly or iterated to converge to the equilibrium distribution because the redistribution of voltage with the director variation is instantaneous.

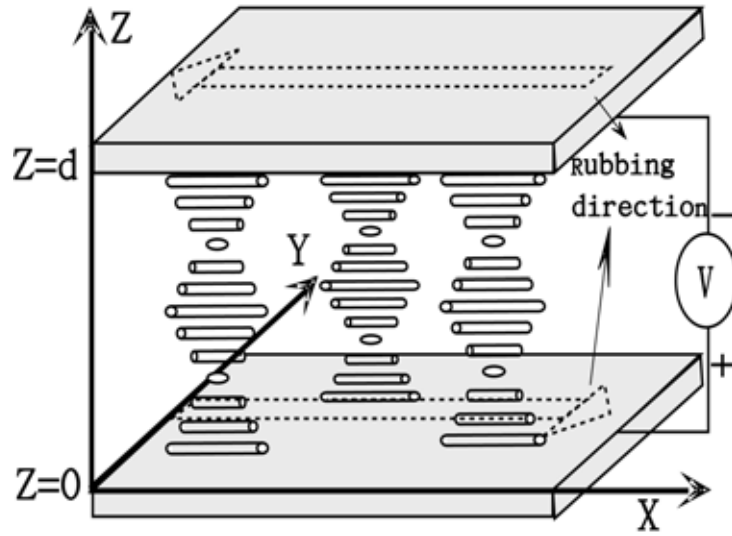


Figure 3.1 Schematic diagram of the cell structure and the coordinate axes.

In this simulation, we use periodic boundary conditions in the x and y directions. Dirichlet boundary conditions are assumed for the planes  $Z = 0$  and  $Z = d$  corresponding to strong anchoring. The cell structure and the coordinate axes are shown in Fig. 3.1. The liquid crystal molecules are initially in the homeotropic texture under an applied electric field larger than  $E_c = \pi^2 / P_0 \sqrt{K_{22} / \epsilon_0 \Delta \epsilon}$ , as shown in Fig. 3.2 [4,11]. When the electric field is turned off, some random noise is superposed on the initial stage, and the liquid crystal relaxes to the planar state. In the simulation, the following parameters are used:  $K_{11} = 8.86$  pN,  $K_{22} = 4.17$  pN,  $K_{33} = 9.28$  pN,  $\Delta \epsilon = 8.8$ ,  $\epsilon_{\perp} = 5.51$ ,  $\gamma_1 = 0.133$  Pas,  $P_0 = 2.247$   $\mu\text{m}$ , cell gap  $d = 5.0$   $\mu\text{m}$ , and pretilt angle =  $3.0^\circ$ . The thickness-to-pitch ratio ( $d/P_0$ ) is 2.225. The rubbing direction is along the x axis. The ranges calculated along the x and y directions are both 5.0  $\mu\text{m}$ .

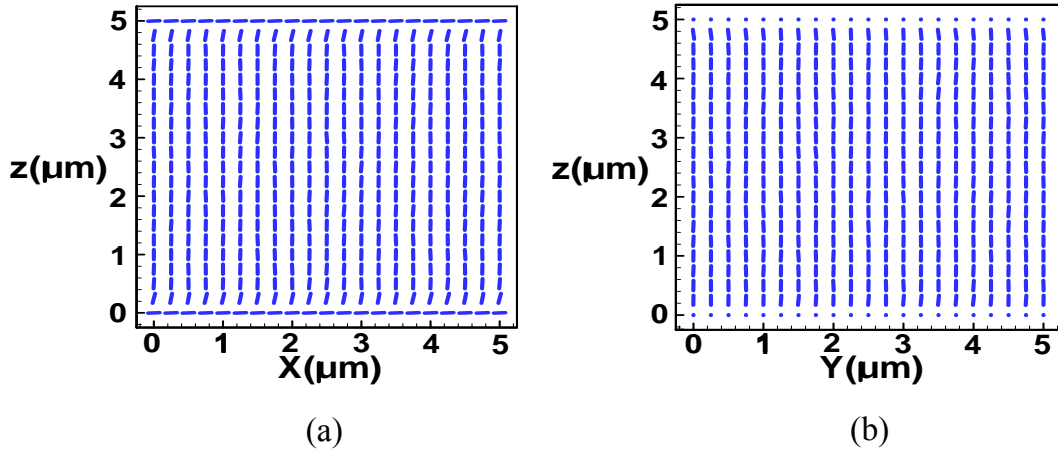


Figure 3.2 Director configurations of the field-induced homeotropic texture. (a) Drawings of the simulated director configuration along Y axis. (b) Drawings of the simulated director configuration along X axis.

### 3.3 Dynamics of the homeotropic to planar texture transition

Figures 3.3-3.7 show the dynamic processes of the transition from the homeotropic texture to planar texture. Here, we show X-Z and Y-Z planes for the three-dimensional director configurations. If the electric field is turned off from the homeotropic texture, the liquid crystal molecules go through one-dimensional conical relaxation to the transient planar texture, as shown in Fig. 3.3. Figure 3.4 shows the transient planar texture with the effective pitch  $P^* = 5.0 \mu\text{m}$  which matches the theoretical prediction,  $(K_{33}/K_{22})P_0$ . The thickness-to-effective-pitch ratio ( $d/P^*$ ) is 1. Due to the high twist energy, the liquid crystal molecules proceed through a three-dimensional Helfrich-like undulation during the transition from transient planar texture to planar texture [12]. The three-dimensional simulation results also clarify another important issue that the three-dimensional Helfrich-like undulation appears even for the low  $d/P_0$  value [6]. Initially, the release from the high twist energy along the rubbing direction will be more apparent than that

perpendicular to the rubbing direction, as shown in Fig. 3.5. The amplitude of the undulation will increase with time. The light transmittance through the system consisting of the three-dimensional deformed layer placed between crossed polarizers is calculated by the Jones matrix method. The light incident on the liquid crystal layer is assumed to be linearly polarized with the polarization direction making an angle  $45^\circ$  with the rubbing direction. Figure 3.6(a) shows the experimental observation for striped undulation along the rubbing direction and small sinusoidal deformation perpendicular to the rubbing direction. This phenomenon is also observed in the simulation result during the transition from the transient planar texture to planar texture, as shown in Fig. 3.6(b) [6]. After the complex three-dimensional bulk modulation, the final equilibrium texture appears, as shown in Fig. 3.7, which displays the two-dimensional planar texture with the intrinsic pitch  $P_0$  and the domain wall.

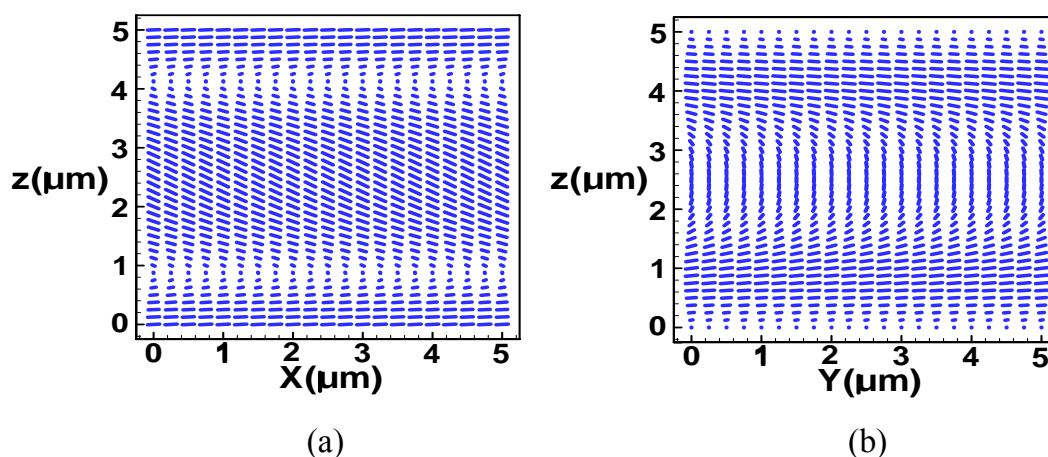


Figure 3.3 Director configurations of the one-dimensional conical relaxation. (a) Drawings of the simulated director configuration along Y axis. (b) Drawings of the simulated director configuration along X axis.

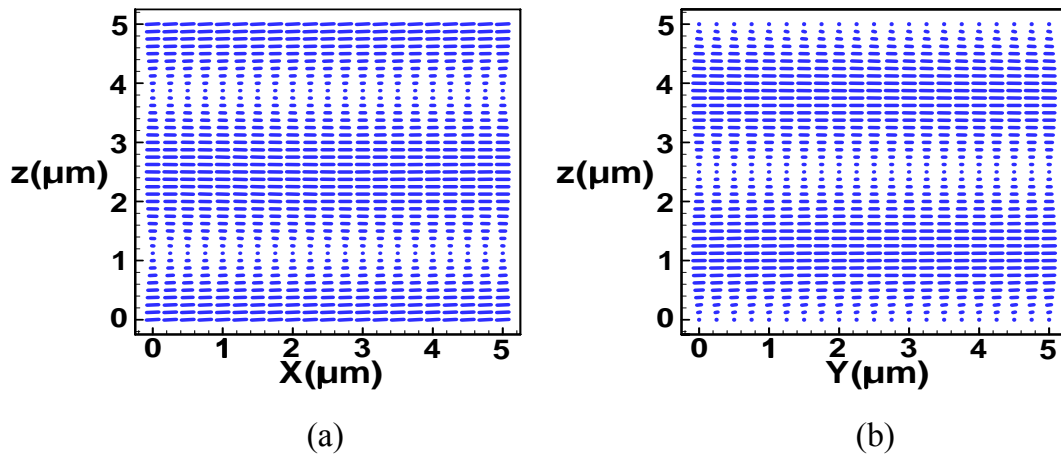


Figure 3.4 Director configurations of the transient planar texture with the  $d/P^*$  ratio = 1. (a) Drawings of the simulated director configuration along Y axis. (b) Drawings of the simulated director configuration along X axis.

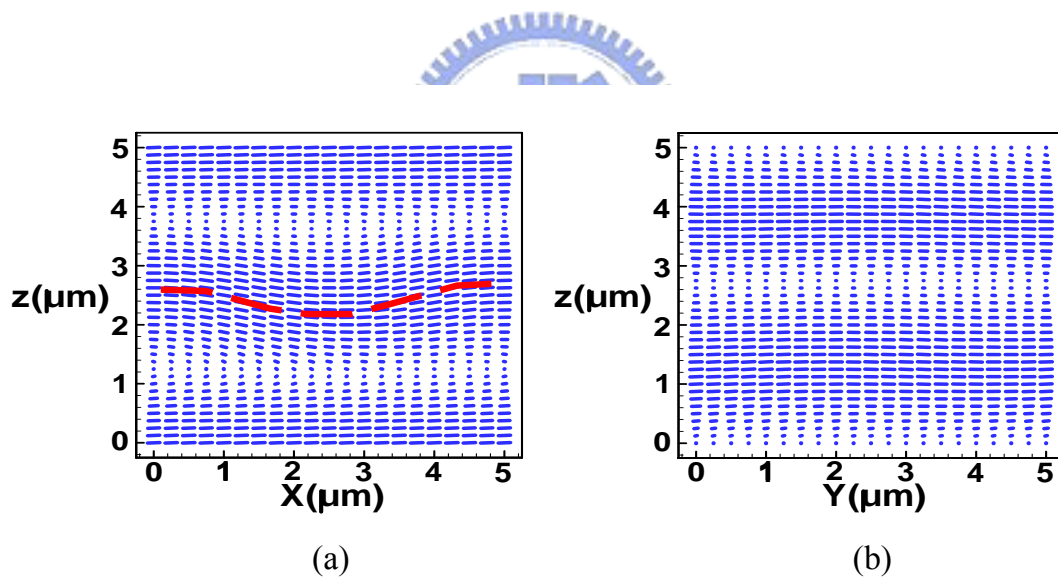


Figure 3.5 Director configurations of the Helfrich-like deformation. (a) Drawing of the simulated director configuration in the medium XZ plane. Dashed line represents the undulation of Helfrich-like deformation. (b) Drawing of the simulated director configuration in the medium YZ plane.

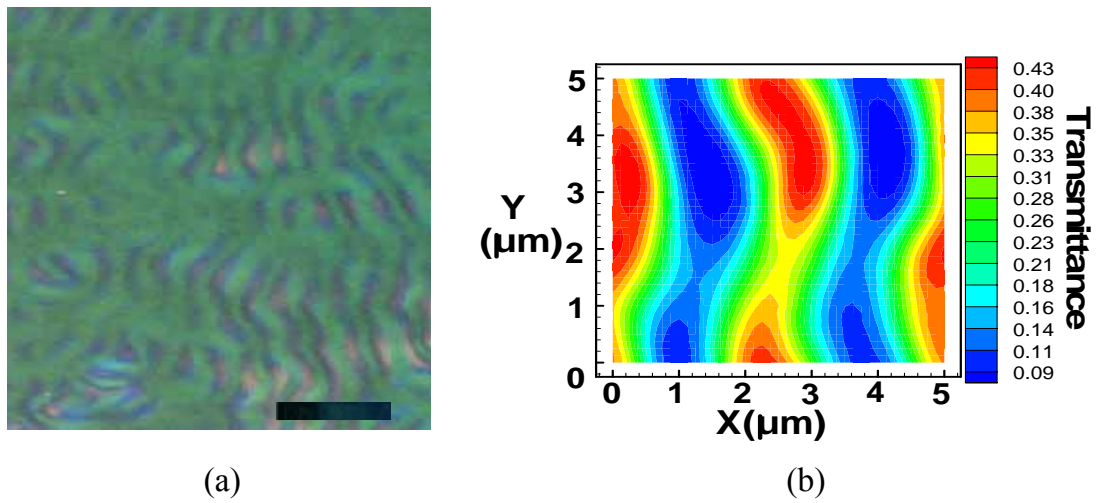


Figure 3.6 (a) Experimental observation of the striped undulation; the black bar is  $25 \mu\text{m}$  long. (b) Transmittance distribution calculated by the  $2 \times 2$  Jones matrix method for the Helfrich-like deformation during the transition from transient planar texture to planar texture.

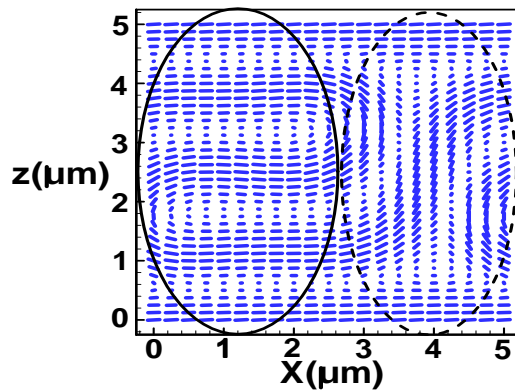


Figure 3.7 Director configuration of the equilibrium planar state with  $d/P_0$  ratio = 2. Solid oval-shaped line represents the planar domain and dashed oval-shaped line represents the domain wall.

### 3.4 Improvements in the response time

Due to the slow relaxation from homeotropic texture to planar texture, a number of methods have been suggested by Anderson, et al. to improve the transition speed [13]. They reduced the high applied voltage to a bias voltage to improve the transition speed during the transition from the homeotropic texture to Helfrich-like deformation. Here, we suggest another way for speeding up the transition. We apply a bias voltage (less than  $V_{PC} = d\sqrt{2}(F_{SC} / d\epsilon_0\Delta\epsilon)^{1/2}$ ) to the cell during the transition from the transient planar texture to Helfrich-like deformation, where  $V_{PC}$  is the threshold voltage for the transition from planar texture to focal-conic texture and  $F_{SC}$  is surface free energy density in the focal-conic texture [14]. From our simulation results, we find that the bias voltage will hinder the relaxation from the homeotropic texture to transient planar texture, but it will accelerate the nucleation process during the transition from the transient planar texture to Helfrich-like deformation. The nucleation speed will increase with the applied voltage. In addition, the impurities or defects will also accelerate the slow nucleation process during the transition from the transient planar texture to Helfrich-like deformation.

### 3.5 Conclusions

By using the three-dimensional finite element method, the details of the transition from the homeotropic texture to planar texture are simulated. The simulation reproduces the observed relaxation from the homeotropic texture to the long-pitch transient planar texture. The simulation also agrees with the suggestion that the transient planar-planar transition occurs via a three-dimensional Helfrich-type deformation without the introduction of defect cores. We hope to enable the rapid updating of cholesteric displays by our simulation results. Two methods of decreasing the time required have been suggested due to the slowness of



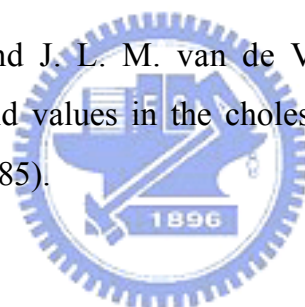
the nucleation process during the transient planar-planar transition. One involves applying a bias voltage to the cell during the transition from transient planar texture to Helfrich-like deformation. The other involves doping a number of spacers or impurities to accelerate the nucleation process.



## References

- [1] T. Yamaguchi, H. Yamaguchi and Y. Kawata: “Driving voltage of reflective cholesteric liquid crystal displays” *J. Appl. Phys.* **85** 7511 (1999).
- [2] D.-K. Yang, J. L. West, L.-C. Chien and J. W. Doane: “Control of reflectivity and bistability in displays using cholesteric liquid crystals” *J. Appl. Phys.* **76** 1331 (1994).
- [3] J.-J. Wu, Y.-S. Wu, F.-C. Chen and S.-H. Chen: “Formation of phase grating in planar aligned cholesteric liquid crystal film” *Jpn. J. Appl. Phys.* **41** L1318 (2002).
- [4] P. G. de Gennes and J. Prost: *The Physics of Liquid Crystals* (Clarendon Press, Oxford, 1993) 2nd ed.
- [5] D.-K. Yang and Z.-J. Lu: “Switching mechanism of bistable reflective cholesteric displays” *SID 95 Dig. Tech. Pap.* **26** 351 (1995).
- [6] P. Watson, J. E. Anderson and P. J. Bos: “Twist-energy-driven Helfrich modulations in cholesteric liquid crystals illustrated in the transient-planar to planar transition” *Phys. Rev. E* **62** 3719 (2000).
- [7] Y.-C. Yang, M.-H. Lee, J.-E. Kim, H. Y. Park and J.-C. Lee: “Theoretical study on the homeotropic-transient planar transition of cholesteric liquid crystals” *Jpn. J. Appl. Phys.* **40** 649 (2001).
- [8] D.W. Berreman: “Dynamics of liquid-crystal twist cells” *Appl. Phys. Lett.* **25** 12 (1974).
- [9] D. W. Berreman: “Numerical modeling of twisted nematic devices” *Philos. Trans. R. Soc. London Ser. A* **309** 203 (1983).

- [10] H. Mori, E. C. Gartland, J. R. Kelly and P. J. Bos: “Multidimensional director modeling using the Q tensor representation in a liquid crystal cell and its application to the  $\pi$  cell with patterned electrodes” *Jpn. J. Appl. Phys.* **38** 135 (1999).
- [11] P. G. de Gennes: “Calcul de la distorsion d’une structure cholesterique par un champ magnetique” *Solid State Commun.* **6** 163 (1968).
- [12] W. Helfrich: “Deformation of cholesteric liquid crystals with low threshold voltage” *Appl. Phys. Lett.* **17** 531 (1970).
- [13] J. E. Anderson, P. Watson and P. J. Bos: “Study of relaxations in cholesteric liquid crystals after reduction of an electric field” *Liq. Cryst.* **28** 945 (2001).
- [14] H. A. Van Sprang and J. L. M. van de Venne: “Influence of the surface interaction on threshold values in the cholesteric-nematic phase transition” *J. Appl. Phys.* **57** 175 (1985).



# Chapter 4

## Transient Phenomenon during the Homeotropic to Planar Texture Transition

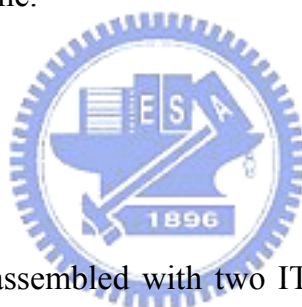
### 4.1 Introduction

Cholesteric liquid crystals with positive dielectric anisotropy exhibit two stable states at zero electric field. One is the Bragg reflecting planar (P) texture in which the helical axis is perpendicular to the cell surface. The other is the scattering focal-conic (FC) texture in which the helical axis is more or less parallel to the cell surface. Switching from P to FC requires the application of a small electric field, but the reverse is not true. Switching from FC to P requires the application of a high electric field which forces the liquid crystal molecules into a homeotropic (H) texture. On removal of the field, a transition from H texture to P texture (H-P) takes place. However, this relaxation is usually slow. For a cell with planar alignment layers, the relaxation process involves a fast conical relaxation to a transient planar (TP) texture, followed by a Helfrich-like deformation which results in the overlap of cholesteric layers to form the P texture [1]. The TP texture is a metastable state with the effective pitch  $P^* = (K_{33} / K_{22})P_0$ , where  $K_{33}$  and  $K_{22}$  are the bend and twist elastic constants of LC materials and  $P_0$  is the intrinsic pitch [2]. The driving force of Helfrich-like deformation results from the high twist energy in the TP texture and the period of that is  $[P_0 d(3K_{33} / 2K_{22})^{1/2}]^{1/2}$ , where  $d$  is the cell thickness [3-5].

In order to use cholesteric liquid crystal displays for video application, considerable efforts have been devoted to reducing the long H-P relaxation time. The effect of surface alignment layers on the H-P relaxation time was described by Gandhi et al [6]. Xu et al. decreased the H-P relaxation time by changing the liquid crystal material parameters [7]. Though the effect of bias voltage on the H-P relaxation process has been studied over a long period of time, improving the H-P relaxation time by designing a driving waveform has not been realized yet [8-11]. In this chapter, we simulate the dynamics of H-P relaxation by using our multi-dimensional simulation software. Furthermore, we study the effect of bias waveforms on the H-P relaxation process. Finally, we design a bias waveform to reduce the H-P relaxation time.

## 4.2 Experiment

### 4.2.1 Cell preparation



The empty cells were assembled with two ITO-coated glass plates. Figure 4.1 shows the flow chart of preparation processes for the empty cells. The substrates were cleaned and ITO-patterned with photolithography. Then they were coated with a 700~800 Å thick SE-3310 (Nissan Chemical Industries, LTD.) alignment layer. We pre-cured the polyamide for 15 minutes at 80°C to smooth the surface and exhaust the solvent, and then hard-cured it for 60 minutes at 300°C for imidization. The substrates with hard-cured polyimide were then rubbed to produce the alignment characteristic of liquid crystal molecules. Figure 4.2 shows the top and side view of the rubbing process. The rubbing density used in this process is about 30. Here the rubbing density is defined as

$$\text{Rubbing density: R.D.} = \frac{3.14 \times B \times C - A}{A},$$

where

A: Moving speed of the substrate support (cm/min)

B: Rotary speed of the roll (rpm)

C: Roll diameter + cloth thickness $\times$ 2 (cm).

It produces a pretilt angle of  $4^\circ$  for liquid-crystal molecules after the rubbing process.

The conditions of alignment-layer processes are listed as follows:

Alignment-layer Process	Condition
Coating	Spin coating method
Pre-curing	80°C/15 min.
Curing	300°C/60 min.
Rubbing	Rubbing roll Rubbing Cloth: Rayon Rubbing density: 30

After the rubbing process, the 6  $\mu\text{m}$  spacers were spread on the substrate to maintain the cell gap and the two substrates were assembled by heat seal, such that the rubbing directions were anti-parallel and the cell spacing was measured to be 6.4  $\mu\text{m}$  by an interferometer. The injected liquid-crystal material was the mixture of 97 % ZLI-4792 (Merck Co.) doped with 3 % chiral agent S811 (Merck Co.), which resulted in a quiescent pitch  $P_0 = 2.98 \mu\text{m}$ , and in turn, the thickness-to-pitch ratio ( $d/P_0$ ) of 2.15. After the LC mixture was injected, the injection hole was sealed with AB sealant.

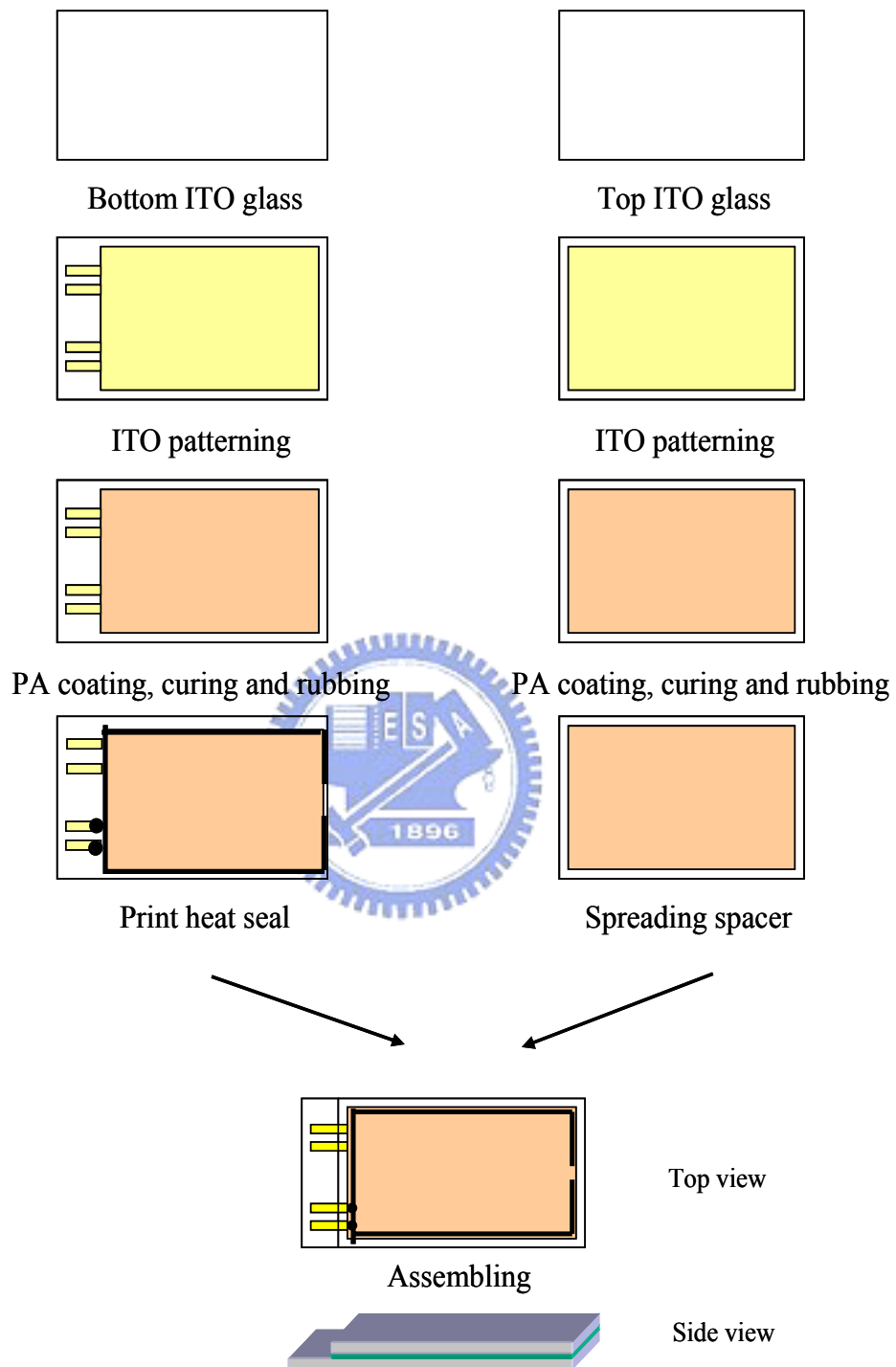


Figure 4.1 Flow chart of the empty cell preparation.

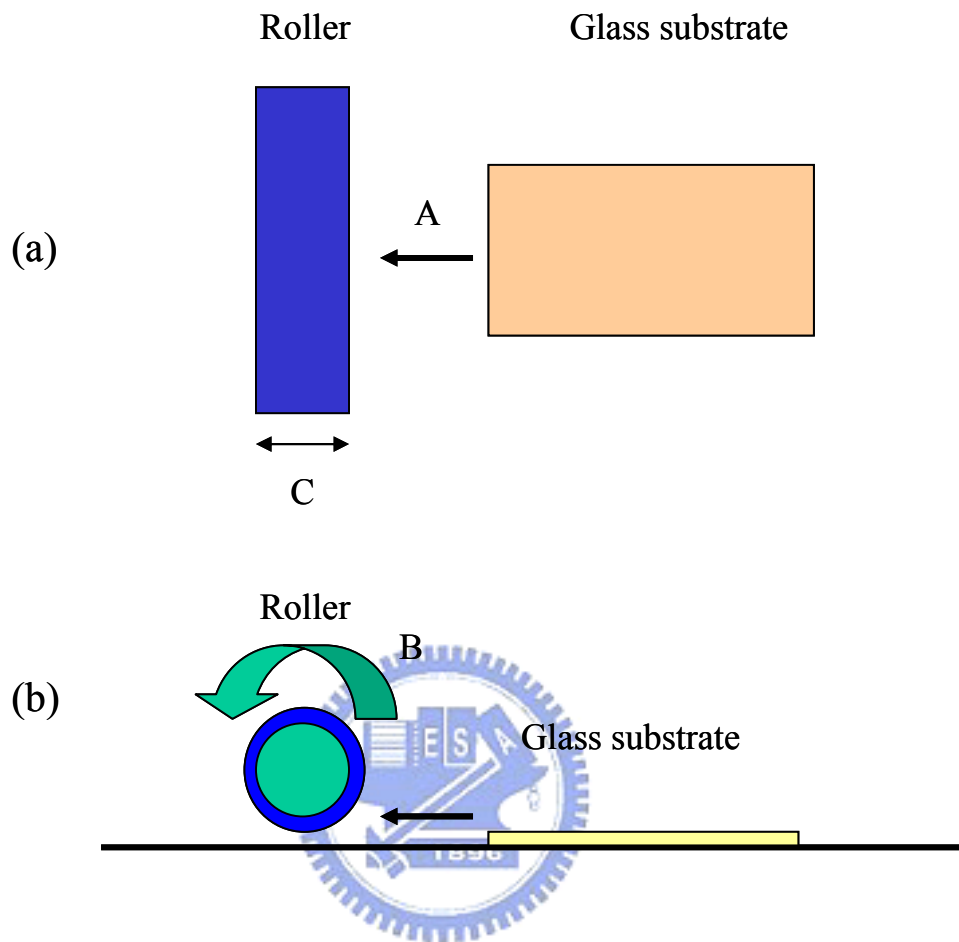


Figure 4.2 Rubbing diagrams of (a) top view and (b) side view, where A is the moving speed of substrate, B is the rotary speed of roller and C is the diameter of the roller.



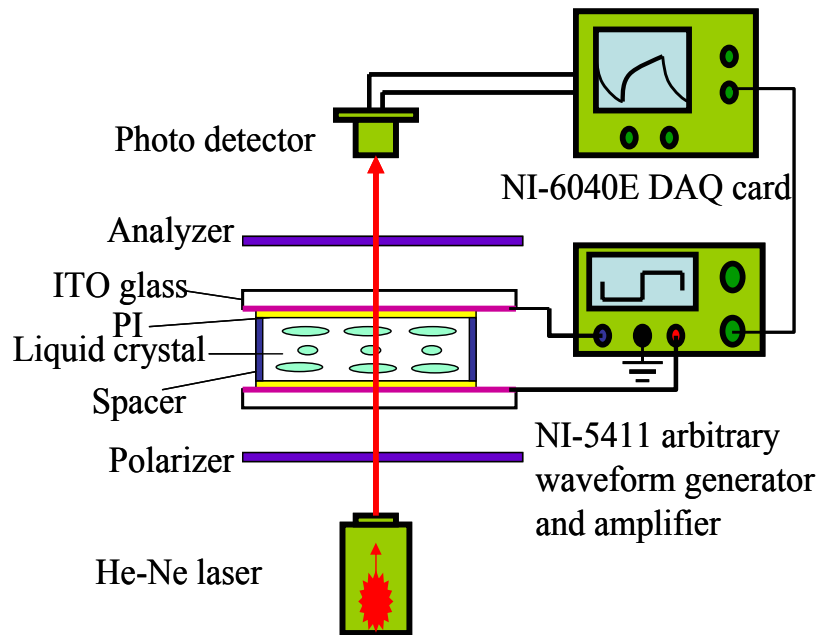


Figure 4.3 Experimental setup.

#### 4.2.2 Experimental procedures

The dynamic process of H-P relaxation is studied by monitoring the evolution of transient transmittance during this relaxation. The experimental setup is shown in Fig. 4.3. The cell is inserted into parallel polarizers and a He-Ne laser light beam is incident on it. The voltage applied to the sample is in the form of a 1k Hz square wave generated by a NI-5411 arbitrary waveform generator and the square wave is routed through a linear amplifier. Both the applied voltage and transmitted intensity are measured using a NI-6040E DAQ card. The temporal resolution of our measurement is 10  $\mu$ s. In this experiment, we applied a voltage of 60 Vrms for 0.5 s to achieve a homeotropic texture and then achieved a relaxation to the planar texture under the application of a bias waveform.

### 4.3 Simulation method

For the modeling of the ChLC system, we use a similar simulation method to that introduced in section 3.2 [12]. In this simulation, the LC material parameters described in section 4.2.1 are used :  $K_{11} = 13.2$  pN,  $K_{22} = 6.5$  pN,  $K_{33} = 18.3$  pN,  $\Delta\varepsilon = 5.2$ ,  $\varepsilon = 3.1$ ,  $\gamma_1 = 0.133$  Pas, and  $P_0 = 2.98$   $\mu\text{m}$ . The physical size of the cell in the calculation is assumed to be  $9.4$   $\mu\text{m}$  and  $6.4$   $\mu\text{m}$  in the X and Z directions, respectively with  $95 \times 65$  node points. Fixed homogeneous boundary conditions are assumed with a  $4.0^\circ$  pretilt angle. In order for the undulation deformation to occur, some perturbations are required to be included in the system. So, the initial director configuration  $\bar{n} = (0,0,1)$  is modified by setting a small random deviation from the cell normal. This results in the random distribution of director components  $n_x$  and  $n_y$  between  $-0.05$  and  $0.05$  and the director component  $n_z$  can be determined based on the relationship  $n_z = (1 - n_x^2 - n_y^2)^{1/2}$ .

### 4.4 Effect of the bias voltage on the homeotropic to planar texture transition

In this section, the influence of the bias waveform on the evolution of transient transmittance during the H-P relaxation is studied experimentally. To understand the relaxation process, the defect-free dynamic process of H-P relaxation is simulated. Figure 4.4 shows the two-dimensional dynamic process of H-P relaxation after the electric field is switched off. The detailed mechanism of H-P relaxation has been discussed in section 3.3 [12]. Figure 4.5 shows the dynamic response of H-P relaxation, which is measured as transmittance versus time after the voltage is removed. While a high voltage of  $60$   $V_{\text{rms}}$  is applied to the cell, the LC molecules are aligned into the H texture and the maximum transmittance is obtained.

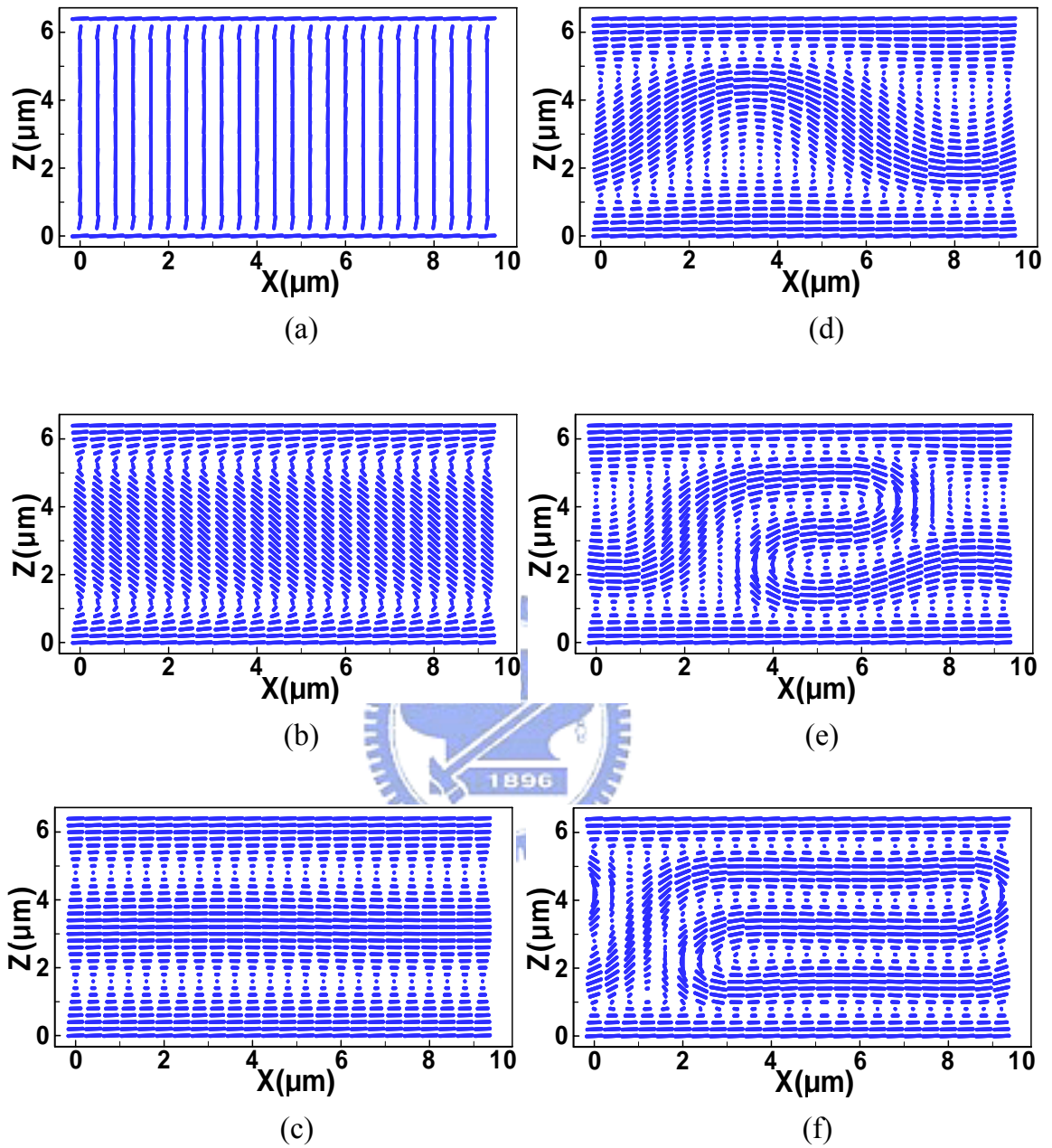


Figure 4.4 Drawings of the simulated director configuration throughout the homeotropic to planar texture transition after the applied voltage is removed.

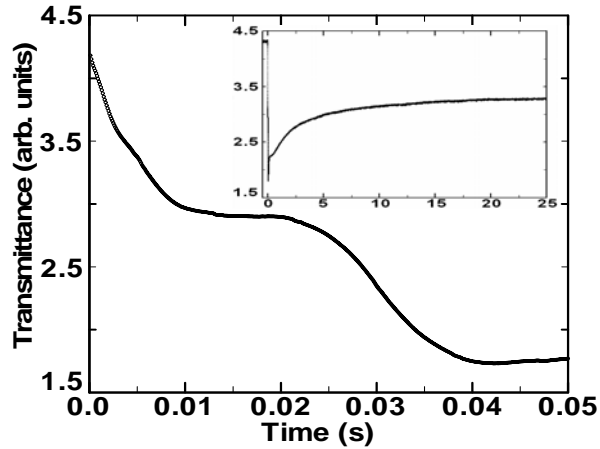


Figure 4.5 Transmittance vs. time during the homeotropic to planar texture transition after the applied voltage is removed. The insert shows the long-time behavior of transmittance.

We will define time  $t = 0$  as the time at which the voltage is removed. According to our measurement results, the LC molecules relax to TP state in approximately 10 ms. The decrease in transmittance results from that LC molecules proceed with one-dimensional conical relaxation. The transmittance does not change for the next 10 ms. This indicates that the LC molecules will stay at TP state for approximately 10 ms. Although the TP state is a metastable state, random fluctuation which is conceived of thermal agitation will nucleate to force LC directors to initiate the Helfrich-like deformation. In our simulation, this thermal vibration is represented as small random distribution in the director profile. The Helfrich-like deformation scatters incident light and results in the decrease in transmittance between times  $t = 20$  to  $40$  ms. This result agrees with the expected Helfrich-like deformation in the simulation. After the Helfrich-like deformation, most LC molecules are slowly aligned back to cell surfaces after  $t = 40$  ms and this results in the slow increase in the transmittance. The slow increase in the transmittance, as shown in the insert of Fig. 4.5, is consistent with the fact that the TP-P transition is a nucleation process.

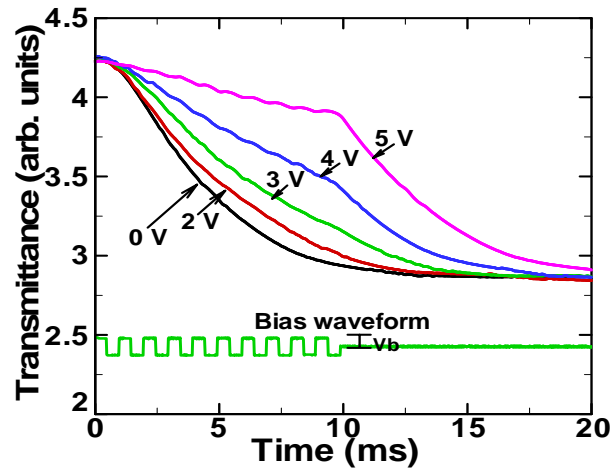


Figure 4.6 Transmittance vs. time during the homeotropic to transient planar texture transition under various bias waveforms ( $V_b = 0 V_{rms}, 2 V_{rms}, 3 V_{rms}, 4 V_{rms},$  and  $5 V_{rms}$ ).

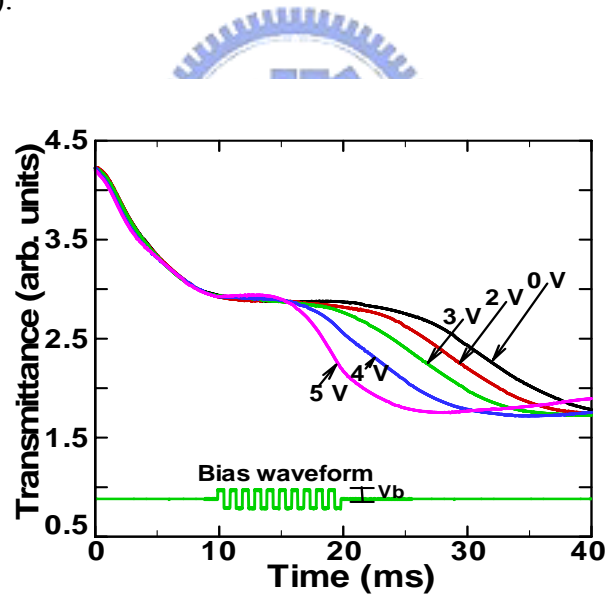


Figure 4.7 Transmittance vs. time in the transient planar texture under various bias waveforms ( $V_b = 0 V_{rms}, 2 V_{rms}, 3 V_{rms}, 4 V_{rms},$  and  $5 V_{rms}$ ).

To speed up this relaxation, we investigate the dynamic response of H-P relaxation by applying different bias waveforms. Figure 4.6 shows the effect of bias voltage on the H-TP relaxation between times  $t = 0$  to 10 ms. The relaxation time increases with bias voltage because the applied bias voltage hinders the conical relaxation from H texture to TP texture. When the bias voltage is higher than  $V_{HP*} = (2/\pi)(K_{22}/K_{33})^{1/2}V_C$  (which is the critical voltage for H-TP texture transition and the experimental value is  $5 V_{rms}$  for this cell), the H-TP texture transition becomes impossible [2,11]. Figure 4.7 shows the influence of bias voltage on the nucleation process in the TP texture between times  $t = 10$  to 20 ms. As the bias voltage is increased, the time for out of the TP texture decreases because the applied voltage enhances the thermal fluctuation. As shown in Fig. 4.8, the bias voltage is applied after the time ( $t = 20$  ms) for Helfrich-like distortion to begin. The time for achieving the maximum Helfrich-like distortion decreases as the bias voltage is increased between times  $t = 20$  to 40 ms. This is consistent with that the amplitude of Helfrich-like distortion increases as the bias voltage is increased. However, the time to form the equilibrium P texture increases with the bias voltage after  $t = 40$  ms, since the bias voltage hinders the LC directors from lying in the plane of the substrates. If the bias voltage is higher than  $V_{P*C}$  (which is the critical voltage for TP-FC transition and is  $3 V_{rms}$  for this cell), the LC directors transform into the scattering FC texture and the time for TP-FC texture transition decreases with the applied bias voltage.

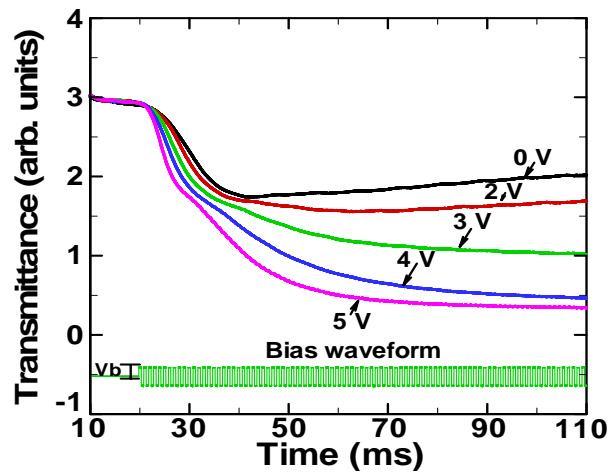


Figure 4.8 Transmittance vs. time during the transient planar to planar texture transition under various bias waveforms ( $V_b = 0 V_{\text{rms}}$ ,  $2 V_{\text{rms}}$ ,  $3 V_{\text{rms}}$ ,  $4 V_{\text{rms}}$ , and  $5 V_{\text{rms}}$ ).

#### 4.5 Driving scheme

Now that we have an understanding of the effect of bias voltage on the H-P relaxation process, we can design a bias waveform, as shown in Fig. 4.9, to decrease the relaxation time required. The relaxation time can be reduced by applying the bias voltage to the cell during the transition from the TP texture to the maximum Helfrich deformation. In this work, the ChLC system with low  $d/P_0$  ratio is studied by applying a bias waveform with  $V_B = 5.0 V_{\text{rms}}$  during times  $t = 10$  to  $20$  ms ( $T_B = 10$  ms). Figure 4.10 shows that the relaxation with such a bias waveform is faster than that without a bias waveform. The relaxation time is reduced from 16 s to 4 s.

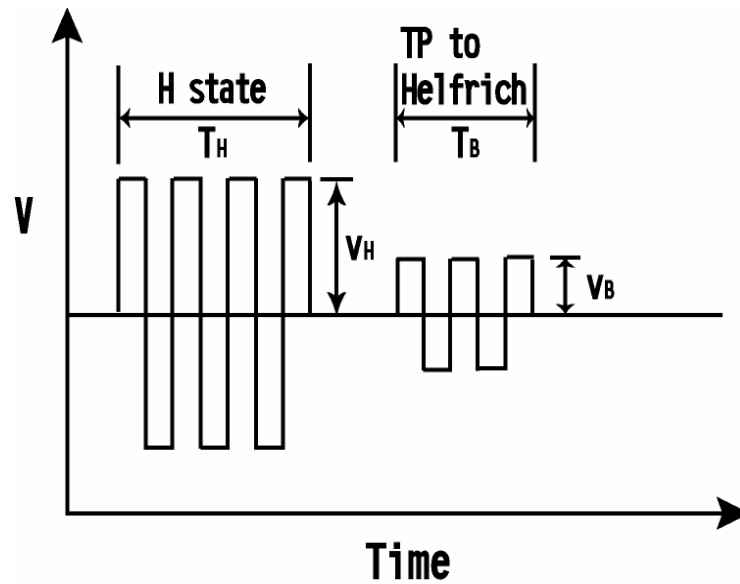


Figure 4.9 Schematic diagram of the bias waveform during the homeotropic to planar texture transition.

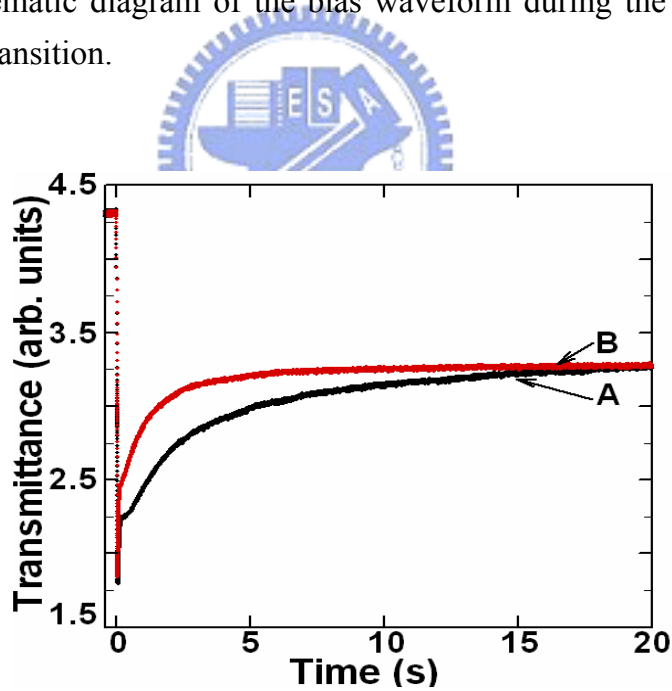
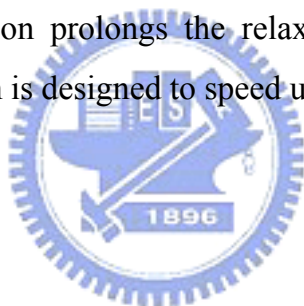


Figure 4.10 Transmittance vs. time during the homeotropic to planar relaxation. Curve A refers to the relaxation curve without a bias waveform. Curve B refers to the relaxation curve with a bias waveform ( $T_B = 10$  ms,  $V_B = 5 V_{rms}$ ).



## 4.6 Conclusions

In this study, we simulated the dynamic process of H-P relaxation using a multi-dimensional simulation program based on the finite element method. By monitoring the evolution of transient transmittance, we observe that the H-P relaxation after the electric field is switched off occurs via a transient planar texture. Moreover, the effect of a bias waveform on the H-P relaxation has also been studied. The time for the H-P transition can be reduced by applying a bias voltage to the cell during the transition from the TP texture to the maximum Helfrich-like distortion. The bias voltage can speed up the nucleation process in the TP texture and can increase the amplitude of Helfrich-like deformation. However, a continuous bias voltage in the H-P relaxation prolongs the relaxation time. On the basis of this knowledge, a bias waveform is designed to speed up the H-P relaxation.



## References

- [1] P. Watson, J. E. Anderson, V. Sergan and P. J. Bos: “Computer simulation of the homeotropic to planar transition in cholesteric liquid crystals” *Liq. Cryst.* **28** 1 (2001).
- [2] D.-K. Yang and Z.-J. Lu: “Switching mechanism of bistable reflective cholesteric displays” *SID 95 Dig. Tech. Pap.* **26** 351 (1995).
- [3] P. Watson, J. E. Anderson and P. J. Bos: “Twist-energy-driven Helfrich modulations in cholesteric liquid crystals illustrated in the transient-planar to planar transition” *Phys. Rev. E.* **62** 3719 (2000).
- [4] W. Helfrich: “Deformation of cholesteric liquid crystals with low threshold voltage” *Appl. Phys. Lett.* **17** 531 (1970).
- [5] J. P. Hurault: “Static distortions of a cholesteric planar structure induced by magnetic or ac electric fields” *J. Chem. Phys.* **59** 2068 (1973).
- [6] J.V. Gandhi, X.-D. Mi and D.-K. Yang: “Effect of surface alignment layers on the configurational transitions in cholesteric liquid crystals” *Phys. Rev. E.* **57** 6761 (1998).
- [7] M. Xu and D.-K. Yang: “Dual frequency cholesteric light shutters” *Appl. Phys. Lett.* **70** 720 (1997).
- [8] S. K. Kwok and Y. Liao: “Transient phenomena of relaxation from electric-field-induced nematic phase to cholesteric phase” *J. Appl. Phys.* **49** 3970 (1978).
- [9] J. E. Anderson, P. Watson and P. J. Bos: “Study of relaxations in cholesteric liquid crystals after reduction of an electric field” *Liq. Cryst.* **28** 945 (2001).

- [10] X.-Y. Huang, D.-K. Yang and J. W. Doane: “Transient dielectric study of bistable reflective cholesteric displays and design of rapid drive scheme” *Appl. Phys. Lett.* **67** 1211 (1995).
- [11] M. Kawachi and O. Kogure: “Hysteresis behavior of texture in the field-induced nematic-cholesteric relaxation” *Jpn. J. Appl. Phys.* **16** 1673 (1977).
- [12] I. A. Yao, J. J. Wu and S. H. Chen: “Three-dimensional simulation of the homeotropic to planar transition in cholesteric liquid crystals using the finite elements method” *Jpn. J. Appl. Phys.* **43** 705 (2004).

